Eidgenössische Technische Hochschule Zürich
Swiss Federal Institute of Technology Zurich

Empa
Materials Science and Technology

Prediction of Temperature Profile and Residual Stress Distribution in Additive Manufactured Parts

Master Thesis

Pooriya Gh Ghanbari

Sunday 7th October, 2018

Advisors: Prof. Dr. E. Mazza, Dr. E. Hosseini

Department of Mechanical and Process Engineering, ETH Zürich

Abstract

Selective laser melting (SLM) is an additive manufacturing process, which uses a high power laser beam to melt certain regions of a powder bed to create a solid part based on CAD data. This build-up process has a high degree of freedom in possible geometries, and if done correctly (i.e. with optimized process parameters) no post-processing would be necessary. SLM, as a sub-category of rapid manufacturing, speeds up the long classical build process. However, this method is not without disadvantaged. As the laser melts metal powder, large temperature gradients develop. Due to thermal strains, residual stresses ensue, which have adverse effects such as distortion, cracking, and reduction of mechanical integrity of the final product. Through process optimization, these stresses can be minimized.

Process parameter optimization is usually conducted through trial and error, which is a lengthy and costly process. Finite element simulations can provide insight into the nature of the SLM problem, and a verified model can be an asset to finding the optimal parameters for minimizing the residual stresses.

In this work, a finite element model is developed for prediction of temperature profiles and residual stresses in SLM parts. Various sensitivity analysis is performed to reach a reliable and representative reference model. With the resulting set of assumptions, a parametric study is conducted and the results are compared with prior studies. Last but not least, an experiment was designed to measure the in-situ temperature during the SLM process by instrumenting the printed parts with K-type thermocouples. The results were used for model verification.

Acknowledgements

I would like to thank my advisor, Dr. Ehsan Hosseini who guided me through each and every step of the project. Thanks to Professor Edoardo Mazza, I was able to work on this project in the High Temperature Integrity Group at Empa Dübendorf under the supervision of Dr. Holdsworth.

In addition, I would like to thank Dr. Leinenbach who collaborated in this project by providing the selective laser melting 3D printing machine, and Mr. Griffiths who helped with printing and preparation of the parts. Furthermore, I would like to thank Mr. Stutz who provided the measurement device.

Last but not least, I would like to thank Mr. Bürki who provided technical assistance during the project, and all the PhD students who did not hesitate to show their support. Finally, I would like to express my utmost gratitude to my family who have provided unrelenting support and encouragement during my years of study. I would not have been able to accomplish this feat without your help.

Thank you.

Pooriya Gh Ghanbari

Contents

Chapter 1

Introduction

1.1 Additive Manufacturing

Additive manufacturing (AM) is the computer-controlled process of producing parts by joining layers of raw material based on a 3D model. This name was chosen as the counterpart of subtractive manufacturing, where desired shapes are made out of bulk material through removing the excess parts by machining, milling, grinding, etc. This technique, formerly known as rapid prototyping [1], generally includes other methods such as sand casting that are used for creating first iterations of a product. As technology improved over time, building near net-shape parts out of metal with low porosity became possible. This enabled using the so-called prototypes as final products with little post-processing, and the more relevant term of additive manufacturing was adopted. As mentioned in ASTM standard terminology [2], other expressions such as "additive fabrication, additive processes, additive techniques, additive layer manufacturing, layer manufacturing, and freeform fabrication" have been used as synonymous titles in the literature.

The novelty of additive manufacturing is in the degree of freedom the designers have in proposing complex geometries [3]. With other methods, engineers have to design for manufacturability (DFM). This places major constraints on the possible geometries and increases the number of separate parts that need to be assembled to create complex systems. Additive manufacturing eliminates these limitations, which is extremely useful where an arbitrary shape at low quantities is needed. Two such applications are bone implants in bio-medical applications, and fuel injectors in aerospace engineering. For instance, Abe at al. [4] demonstrated freedom of design of AM by using selective laser melting to create a titanium bone shape with similar tensile strength to pure titanium.

Another advantage of additive manufacturing is its applicability to a wide range of materials such as ceramics, polymers and metals [5]. Since AM

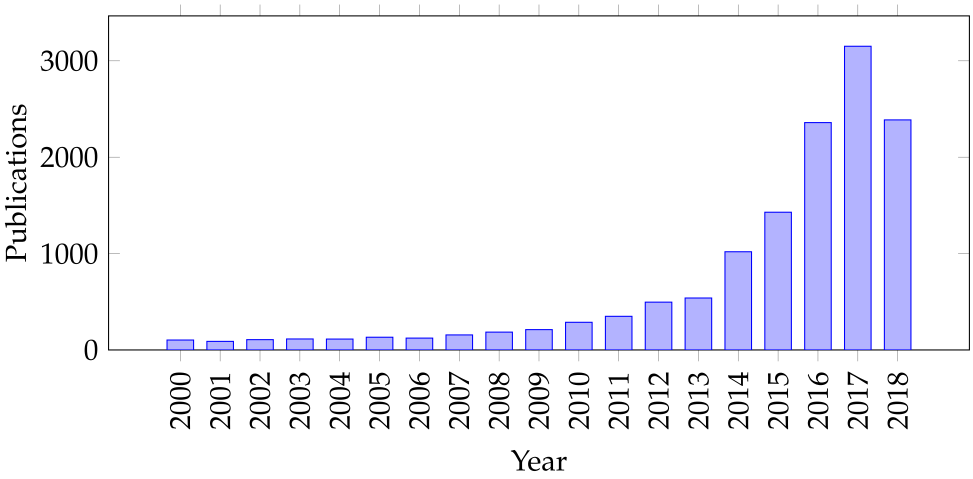

Figure 1.1: Number of publications containing the "Additive Manufacturing" keyword per year. The data was acquired on 24th of September 2018 through Web of Science v5.30.

follows the simple idea of generating parts through deposition and adhesion of layers of raw material, machining issues such as spring back and chatter (mostly with titanium alloys) or shrinkage in casting are absent.

Additional benefits of AM include lower costs at small scale production, less material waste (specially for expensive alloys), and fast prototyping [5, 3]. However, there are still many obstacles in widespread application of AM. Some barriers are poor reproducibility, inferior mechanical properties, limited product size, and complicated optimization due to multiplicity of process variables [5]. Compared to other common methods of manufacturing, it has been rated on the 3rd technology readiness level [6] (TRL is a quantitative expression of the state of a technology regarding widespread commercialization). Fortunately, the research in the field of additive manufacturing is growing rapidly as shown in figure 1.1.

One of the problems with additive manufacturing of metals is the large temperature gradients that develop in the part during the manufacturing process. These high gradients occur because the melt pool is usually small (2 mm width for direct energy deposition [7] of Steel 316L and 100-500 µm for selective laser melting of γ-TiAl alloy [8]) and the melting point of metals is high. Large temperature gradients cause localized expansion of the part. The resulting thermal strains are usually high enough to create plastic deformation, which in itself induces residual stresses in the product. These stresses can cause cracking and delamination during build-up, or distortion after release from the substrate [9, 10]. Furthermore, they have adverse effects on mechanical integrity such as reduced endurance life under cyclic loading [4, 11].

Before discussing selective laser melting (SLM), the classification of AM processes by Williams et al. [12] shall be reviewed in order to illustrate characteristics of SLM compared to the other methods. They classified AM processes based on five attributes, namely: type of raw material, patterning, adhesion, build-up method, and support structures.

1. *Raw material*—can be solid, liquid, or gas. Each of the three has subcategories. For instance, solid can be in the form of single or double phase powder, coated powder, tape, or wire. In this work, single phase solid powder is used for SLM.

2. *Patterning*—is the main subfunction which determines how the parts are built up in each layer. It can be either direct deposition of material, patterning of energy, or both of them at the same time. As a powder-bed forming technique, SLM uses laser to form a pattern on each layer based on CAD data.

3. *Adhesion*—determines how raw material is transformed to the final shape. In all AM processes some form of energy is used to enable phase transition, which can take the form of melting, sintering, polymerization, etc. A high power laser selectively melts metal powder in SLM.

4. *Material addition*—As the part is built up, additional material needs to be added. This can be done either through recoating or simultaneous deposition. In SLM, a thin layer of powder (thickness is on the order of magnitude of size of powder particles) is deposited by a recoater.

5. *Support structures*—fabrication of shapes such as cantilevers, holes, and undercuts requires support structures. Burning, solving, and breakage are the three methods used for the final release. In single phase SLM, these structures are broken as the other two cases more than one phase should be present.

1.2 Selective Laser Melting

Dr. Fockele and Dr. Schwarze of Stereolithographietechnik GmbH in collaboration with the Fraunhofer institute submitted the patent for steel powder-based selective laser melting technology in 1997 [13, 14, 15]. In the standard terminology of ASTM [2], a separate entry for SLM is not defined and this method, alongside selective laser sintering (SLS) both fall under *laser sintering (LS)* definition. This nomenclature is not literal and only has a historical background. In most AM processes including SLM and SLS, partial or full melting of powder occurs. Laser powder bed fusion (LPBF) is another ASTM term that is used to refer to SLM.

As briefly mentioned in the previous section, SLM is an additive manufacturing process where a high power laser melts certain regions of a powder bed based on a sliced CAD model. After deposition of each layer, the build platform is lowered equal to the layer thickness and a recoater blade moves along the surface of the build to deposit a thin layer of powder on top of it. The blade usually sweeps the print area twice in order to achieve a flat surface and remove any excess powder. Once the build process is complete, unmelted powder is removed and the part can be released from the substrate [13].

In addition to manufacturing components, SLM has been used for repairing damage. Acharya et al. have developed a new method called scanning laser epitaxy (SLE) for single crystal turbine blades made of CMSX-4 [16, 17], and two superalloys [18, 19]. They covered the surface of the damaged parts with powder, and used high power laser for melting it, which filled up the pores and cracks on the surface.

In SLM machines, there is a constant flow of a non-reactive gas such as argon, or nitrogen through the printing chamber. Some metal powders such as magnesium are highly reactive, which necessitates a low amount of oxygen in order to avoid burning or oxidation at high temperatures [20, 13]. Additionally, the gas flow carries away some of the excess material from the melt pool due to splattering. Otherwise, the small particles would affect the powder bed stability and flatness [21].

Melt-pool stability depends on scan speed, laser intensity, layer thickness, substrate material, and physical properties of the powder [22]. If liquid metal does not wet the underlying surface, it would solidify as a spherical droplet. This phenomenon, known as “balling” [23] happens due to insufficient wetting. The causes can be either low energy density, or high oxygen content in the chamber and oxidation on the surface of exposed layers [24]. Balling increases porosity and surface roughness [13, 24]. A deformed build surface can interfere with the recoater blade and damage it, or create an uneven powder layer which would affect build-up process of subsequent layers [13].

On the other hand, high energy input increases the melt pool temperature to the boiling point and causes excessive evaporation, splattering and the “keyhole” effect which has been investigated by King et al. [25]. For high energy input, the melt pool temperature rises above the boiling point, and a vapor cavity forms. This increases laser absorption and creates a much deeper melt pool. Collapse of vapor bubbles causes voids and defects in the solid [25].

The energy needed for melting the powder is delivered through laser radiation. Absorptance, defined as radiation absorption divided by the total incident radiation, plays a major role in determining the optimal laser power

Table 1.1: Titanium absorptance in dense and powder form for different laser wavelengths (λ) [26, 27]

Laser wavelength	$\lambda = 1.06\mu m$	$\lambda = 10.6\mu m$
Solid Ti	30	8
Powder Ti	77	59

for an ideal melt pool [13]. While the penetration depth can be in the range of 10 nm–1µm for dense opaque bodies, the light can go through the cavities between powder grains, and increase effective optical penetration depth [13]. Thus, in addition to the radiation absorbed by the top surface of the powder bed, some of the radiation gets absorbed inside the cavities between powder particles [13]. These cavities effectively act like a black body [26], and significantly increase the absorption coefficient for the powder equivalent of the dense materials [13]. As an example, the absorptance of titanium in bulk and powder form is presented in table 1.1.

An inherent aspect of SLM is the development of significantly high temperatures in the melt pool during the build up process [9]. For instance, the melting point of stainless steel 316L has been taken as 1427°C according to Kim [28], and the melt pool temperature for SLM has been reported up to 2200°C [29]. The temperature gradients are in the 10^4–10^5 K/m range [17], and cooling rates have been measured in 10^4–10^5 K/s order of magnitude [9].

Mercelis et al. [9] investigated the residual stresses in selective laser sintering (SLS) and melting (SLM). When the top layer is heated by the laser beam, thermal expansion is restricted by the solid material underneath, and compressive stresses develop in the heated area. As the material strength drops with increasing temperature, and the heated region undergoes thermal expansion, plastic deformations develop in the top layer. After the heating phase and during cool-down, the molten material shrinks. The shrinkage is limited by the surrounding solid underneath the melt pool. Therefore, the top layers fall under tension as compressive stresses develop in layers below [9].

Residual stresses are typically close to the yield strength of the material, and can cause cracking and delamination during the build-up process [10]. Additionally, once the part is removed from the build plate, distortion and warping might occur due to thermal stresses [30, 31]. High deformations can render the part useless and necessitate reprinting with different SLM process parameters and/or scan strategies. Furthermore, residual stresses reduce mechanical integrity of the part, in particular the fatigue endurance

[11].

Some ways to reduce residual stress are finding optimal AM process parameters, and using alternative scan strategies such as island scanning [32, 33, 34]. In addition, post processing measures can be used to enhanced the integrity of the manufactured parts. For instance, Shiomi et al. [35] tried to reduce residual stresses of SLMed SCM440 steel alloy parts in three ways. By heat treating SLM parts for 1 hour at 600°C or 700°C the residual stresses decreased by 70%. Heat treating at 500°C decreased the stress levels by only 10%. They also tried laser re-scanning of each layer during the build-up process. With increasing laser power in re-scanning the top layer residual stresses decreased. For instance, 150% of laser formation energy caused a 55% reduction in residual stresses. Lastly, they preheated the base-plate and powder bed during the buildup process, which reduced the cooling rates. This method decreased the residual stresses by %40 (with 160°C preheating temperature).

1.3 Motivation

While post processing measures can alleviate the issue of residual stresses, spending resources in this area would eliminate the purpose of rapid prototyping. Hence, it is useful to employ optimal SLM process parameters with an efficient scanning strategy. The optimization process is usually done through experiments and statistical analysis [36, 37, 38]. While the concept of SLM is relatively simple (i.e. melting powder to form dense parts), the large number of process parameters affecting the resulted residual stress state makes experimental optimization costly and time consuming [39]. This is where numerical simulations such as finite element method can be of use.

Through simulations, one can evaluate the effect of variations in input parameters (e.g. laser power, scan speed, layer thickness) on output results (e.g. residual stress, temperature profile, distortion) [40]. Once a model is established and verified, it can be used to predict residual stresses and part distortion for different sets of process parameters. Ultimately, this concept would be implemented in an optimization process, and reduce the time and cost of SLM fabrication of desired parts.

In simulating multiphysics processes such as SLM, an accurate model capturing every aspect of the process would face a number of problems. Some parts such as heat convection or radiation often require case by case experimental measurements or complex CFD modeling. Adopting values for these parameters based on literature can become an additional source of uncertainty in the results. Another issue with implementing every detail is the model complexity, and the resulting high computational costs. For instance, due to the small size and fast movement of laser, fine mesh structure and short time increments are required to capture the temperature evolution. Furthermore, the melt motion and surface tension need to be included in order to study the wetting of solid substrate and heat convection in the melt pool. While these phenomena might be of interest for micro-scale investigation, their consideration in a macro simulation (e.g. for a real-size build) is impractical as the simulation times would become extremely long. Therefore, the scope of each model shall be decided beforehand. While in small scale modeling, many physical phenomena and their interactions can be taken into consideration, for large size-scales, should neglect trivial aspects of the problem. A sensitivity analysis might be required for identification of the dominant phenomena and mechanisms.

There have been many attempts at simulation of SLM processes [41, 42, 43, 44, 45, 39, 30, 46, 47], which can be categorized in three groups based on their dimension scale. Khairallah and Anderson [39] studied melting of a randomly generated steel 316 powder bed and its solidification continuity. Dai and Gu [45] investigated the melt pool behavior in SLM of copper composites using finite volume method. They reported 17.5 kJ/m as the optimized laser energy density which produced 96% dense parts. At higher laser powers, the Marangoni flow would entrap the vapor bubbles and increase porosity. Roehling et al. [46] performed simulations to derive the temperature gradients and velocity field of the melt pool to support their experimental work on SLM of steel 316. In these studies, usually only a single track of laser is modeled which includes fluid flow considerations. The focus is the conditions that cause adverse effects such as balling or keyhole formation. Wu et al. [47] created a model for SLM with powder grain, evaporation, and surface tension definition, and supported their simulations with experiments on shape and behavior of the melt pool.

At a slightly larger scale (sometimes referred to as mesoscale) a few layers and tracks of laser are modeled to study their interaction as the high gradient temperature field develops in the system. In these studies, the laser energy distribution and movement is modeled but more complex phenomena such as melt motion are neglected. Dai and Shaw [41] performed thermo-mechanical simulations on bi-component SLM of nickel and ceramic powders. They reported the thermal field, residual stresses, and warpage of parts based on simulations. Hussein et al. [44] investigated the temperature and thermal stress development during SLM process of unsupported structures. Song et al. [43] performed simulations on Ti6Al4V and studied the effect of scan speed on microstructure and build quality both numerically and experimentally.

Finally, real world parts are beyond microns and scale up to centimeters. At macroscale, laser energy field shape, and laser beam movement is not simulated and whether a layer-by-layer melt/deposition or an inherent strain method is used. Despite neglecting laser distribution details, the results have proved to be relatively accurate. For instance, Zaeh and Branner [42] proved the effectiveness of a simplified approach for modeling SLM manufacture of a T-shaped cantilever made out of 1.2709 steel alloy. In their model, layer thickness was 1 mm instead of 50 μm and a constant value of 500 W power was applied to each layer instead of a moving laser. They measured tensile residual stresses using neutron diffractometry up to 435 MPa and compressive residual stresses of -337 MPa. In comparison, their simulation showed residual stress values at 490 MPa in the cantilever. Li et al. [30] used a different approach to macro-scale modeling. They modeled the laser interactions on the micro scale, and used the results to define an equivalent heat source for the larger part with a surface area of 35 mm×15 mm.

In this work, the Abaqus finite element package was used. Among the three dimension scales mentioned above, the mesoscale was chosen since it contains the intricacies of the laser definition, neglects the complications from liquid metal flow, and calculates residual stresses in a reasonable duration of time.

1.4 Outline

The next chapter presents the performed experimental work in this study for the purpose of generation of data for model verification. Chapter 3 explains the developed thermal and mechanical FE model for prediction of temperature profile and residual stress distribution during SLM process. Chapter 4 introduces a reference model and discusses the sensitivity of predicted temperature profile and residual stress development during SLM to different model assumptions. Section 4.3 demonstrates the effectiveness of a simplified approach in comparison with the observations from the "reference" model. Section 4.4 provides a discussion on influence of SLM process parameters on the predicted temperature profiles and residual stresses during the manufacturing process. This chapter ends with verification demonstration of the developed finite element model based on observations from the experiment described in chapter 2. The last part of this dissertation gives the summary and outline of this study.

Chapter 2

Experimental Work

Before going into detail about the finite element model and the simulation results, the conducted experiment in this study is described in this chapter. The results are used in section 4.5 to verify the finite element simulations.

2.1 Objective

The goal of the experiment was to measure the temperatures that develop in the printed part during the SLM process, which were later used to verify the thermal simulations. K-type thermocouples were chosen for the temperature measurements. These thermocouples can measure up to 1200 °C. Thus they were suitable for SLM of steel 316 as long as they were not placed directly under the laser path. A similar approach has been taken in a number of studies. Dunbar et al. [48] placed the thermocouples on the substrate and observed temperatures up to 100 °C during SLM process. This temperature rise was due to the overall heating of the part, and the method could not monitor local temperature increase near the melt pool due to laser beam exposure. In another experiment by Chiumenti et al. [49], the thermocouples were attached to the build part itself. They first printed two walls (both 80 mm in length but with different thicknesses of 5 and 40 mm) up to 20.24 mm. After stopping the print process and removing the excess powder, they attached the thermocouples. Afterwards, they put the part back in the SLM machine to print another 29.76 mm on top of it. The thermocouples were not welded to the part, and were just placed inside holes at the side of the walls. The maximum measured temperature in their study was 200 °C which is higher than the previously mentioned study. Additionally, the temperature peaks corresponding to the laser beam were sharper in [49].

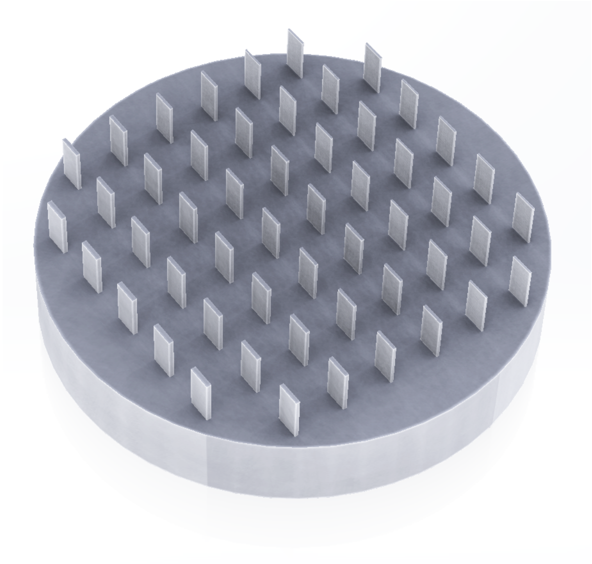

Figure 2.1: Arrangement of thin structures with varying thicknesses.

2.2 Steps

A two phase print procedure was considered following a similar approach to Chiumenti et al. [49]. Thin walls of thickness and up to a height of 10mm were printed out of stainless steel 316 powder (figure 2.1). Then, the build was extracted to be instrumented by several spot-welded thermocouples before restarting the print process.

The goal was to have as little solid material as possible near the thermocouples to reduce heat capacity and thus increase the observed temperatures. Therefore, the structures were designed with the least possible thickness. Different thicknesses were chosen because there was no information available on the minimum possible feature size with the available machine. The only known information was the laser spot radius of 55µm which meant that a minimum melt pool size of 110µm was to be expected. Additionally, a very thin structure could bend easily during thermocouple welding process. Such bending deformation is problematic for restart of the print process, as the new layers cannot attach to previously solidified material. This creates free moving pieces of solid material, which can be displaced by the recoater blade, and disrupt the print process. Thus no smaller thickness than 400µm was chosen, and they proved to be rigid enough to allow attachment of thermocouples without permanent bending. The printed part after the first stage of the print and before thermocouple attachment can be seen in figure 2.2.

The employed temperature data acquisition equipment was HBM MGCplus

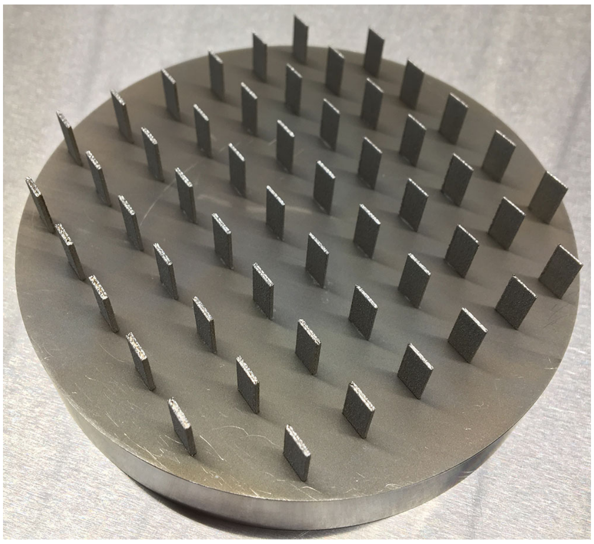

Figure 2.2: Thin structures after the first part of printing.

which had 12 high frequency channels. Four of these channels had a DAQ frequency of 4800Hz while the other eight were limited to 2400Hz. Therefore, the 12 thermocouples were divided into three groups and were attached to three of 400μm thick structures. Two out of four were attached to the edge of the thin wall in order to be as close as possible to the melt pool in the beginning of the print. One thermocouple in each group was placed slightly below the edge, in case the laser would melt the higher two and temperature readings would fail in them (this did not happen and all thermocouples had consistent output throughout the whole process). The last thermocouple was attached to the middle of the structure to monitor the overall temperature change of the part. In figure 2.3 these placements are shown.

After thermocouple attachment, the bare sections of the wires were coated with thermal/electrical resistive black color in order to provide electrical insulation. Otherwise, conductive metal powder could have caused a short circuit between the wires and resulted in erroneous temperature readings.

After the part was instrumented with thermocouples, it was placed into the SLM machine and filled with powder up to the surface of the thin walls. Since there must be no obstacles in the ways of recoater, the wires were all guided through the same side of the substrate and a small part of the recoater was cut in order prevent interference. This caused free moving solid layers to form near the wires, but since that was far from the measured structures, it was not a major concern. The setup for the second print can be seen in figure 2.5.

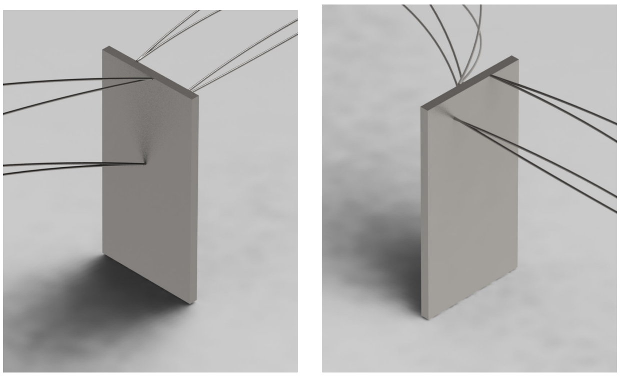

(a) (b)

Figure 2.3: A schematic of thermocouple placement on one of the thin structures. a) Edge and middle thermocouples. b) Edge and top thermocouples.

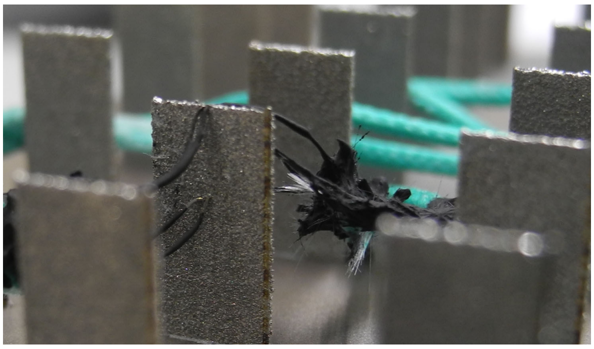

(a) Close-up of thermocouples

(b) Three instrumented structures

Figure 2.4: The printed part after spot welding the thermocouples. a) Thermocouples were spot welded at different locations on the structures. Afterwards, they were colored with thermal/electrical resistive paint. b) Twelve thermocouples after attachment and before final coloring are shown. The wires were glued to the base plate in order to avoid detachment during transportation.

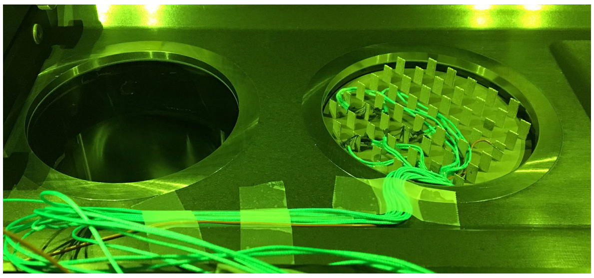

Figure 2.5: Arrangement of thermocouple wires for the second print in the SLM machine.

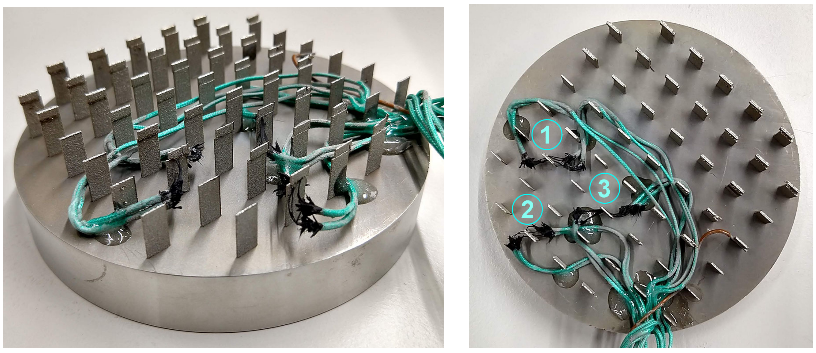

(a) Second print

(b) Top view

Figure 2.6: Due to misalignment, not all structures were successfully printed. a) The result of second print. The three structures with thermocouples had solidified parts on top of them. b) Effect of base plate rotation can be clearly seen on the thicker structures near the edge.

One factor which was not taken into consideration was the precision in placement of the base plate for the second print. The base plate had four holes on its bottom which fixed it to another cylinder through pins. The bottom part itself was screwed in. There was no error in pin attachment, but since the screwing was done manually, it could have been slightly looser or tighter than the first print, thus misplacing the structure. This caused the second print of thin structures close to the edge not to attach at all, and for the thicker ones, the shift could be clearly seen (figure 2.6). A solution to this problem is attaching thermocouples somewhere near the center of the substrate as rotations result in smaller misplacements in this region. Another way is to change the design to concentric circular arcs around the center of the substrate which would not have major problems with misalignment.

Figure 2.7: The scan strategy used for thin walls consisted of two rectangular contours. The outer ones were printed at once before the inner ones for all structures.

2.3 Results

The second print consisted of 66 layers which correspond to a height of 2 mm. The highest data acquisition frequency was 4800Hz, thus sensor outputs were recorded every 208.3µs. This includes even the 2400Hz channels where each data point was recorded twice. During the print process none of the thermocouples failed and they had temperature readings throughout the whole process. However, contrary to expectations and due to the misalignment issue mentioned in the previous section, the edge thermocouple pairs did not measure similar temperatures. The thermocouple labels can be seen in figure 2.8.

In all three cases, one of the edge thermocouples had higher temperatures than the other due to being closer to the laser path as seen in figure 2.9. For the first pair, the structure is the farthest from the center among the three under investigation. Thus the sensor further away from the laser path shows significantly lower temperatures. In case of the second pair, the location is similar to the previous one but the second print is better attached to the previously solidified parts. Therefore, higher temperatures were seen in ET2 (see figure 2.8). Finally, for the last pair which are the closest to the center, the smallest difference is observed. However, the left hand sensor (W) shows a lower temperature compared to its opposite thermocouple which is contrary to the previous cases. This shows that this pair was in the lower half of the base plate, and the laser was closer to the right side thermocouple.

Another point to discuss in figure 2.9 is the double peaks for each deposition. In the slicing of the CAD part, the 400µm structures were printed with two rectangular contours (figure 2.7). In all scanning strategies, the machine first prints the outermost laser path for the whole layer and then starts printing the inner areas. Similarly, here first the outer rectangle for all structures were printed and then they were filled in.

In general the 2400Hz channels had a signal noise of around ±10°C, which masked the signal in two of thermocouples attached at the bottom. The 4800Hz readings had much lower levels of noise. The history for EM1 and WB1 can be seen in figure 2.10

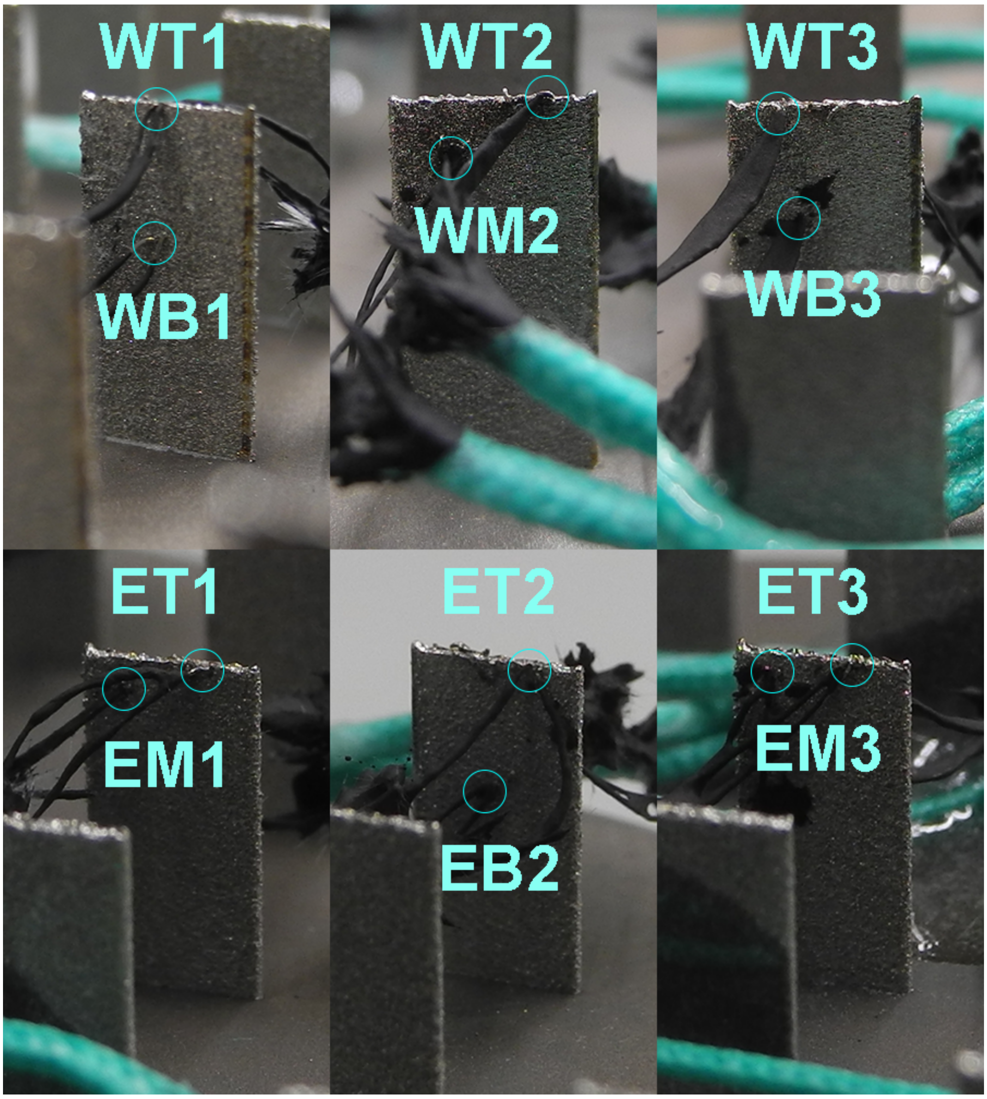

Figure 2.8: Label assignments for the twelve thermocouples. The 1st, 2nd, and 3rd structures have been denoted in figures 2.4b and 2.6b

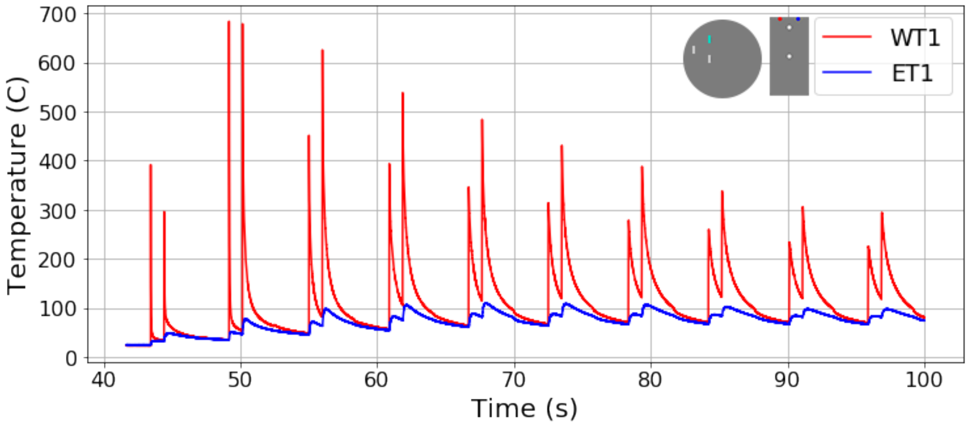

(a) Group 1

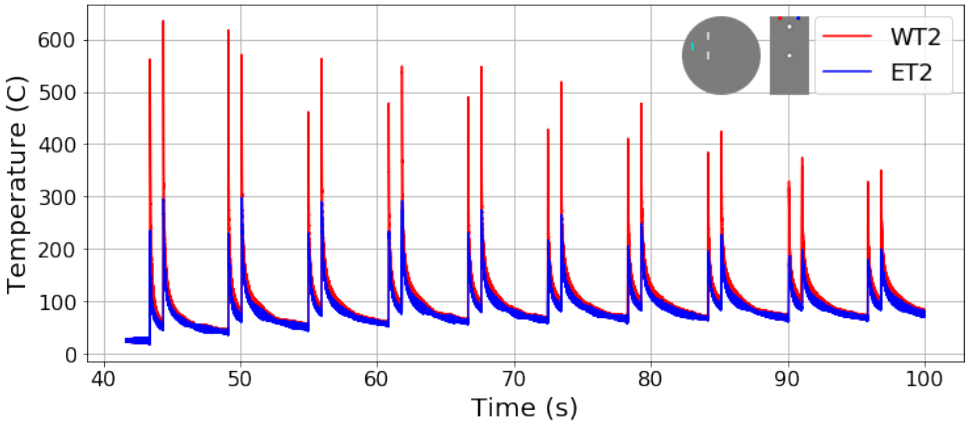

(b) Group 2

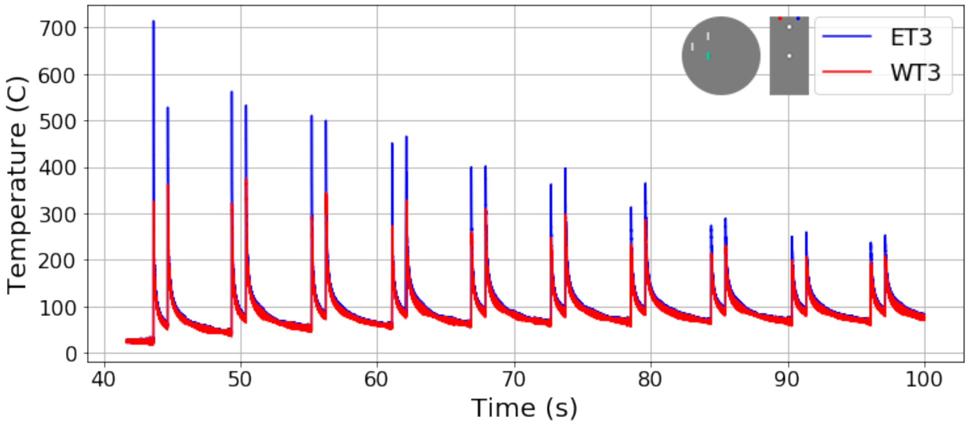

(c) Group 3

Figure 2.9: Temperature history in the six thermocouples placed near the edge during printing of the first ten layers.

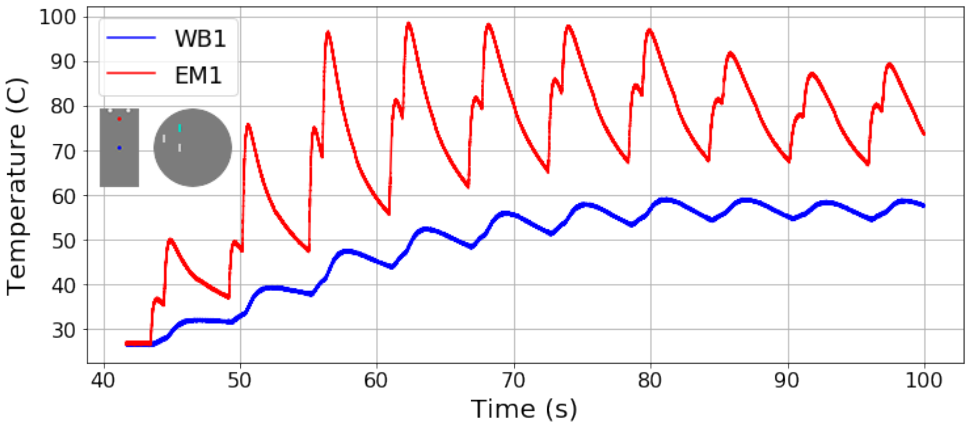

Figure 2.10: Temperature evolution in two thermocouples away from the edge.

Chapter 3

Finite Element Model

Modeling of the SLM process can be summarized in two interactions; I) The heat input from the laser beam melts the powder which solidifies during cool down. II) Due to significant temperature gradients in the heating process, large thermal strains and stresses develop in the part. Based on this problem description, having both thermal and mechanical consideration are necessary for modeling of the SLM process. Such a multiphysics problem requires a coupled analysis, which can be simplified in the form of sequential coupling to significantly reduce the computational costs.

In general, sequentially coupled multiphysics analyses are used when the dependency of present phenomena is important only in one direction. In other words, the governing equations for some of the unknown fields can be solved without knowledge of the other. The most common sequentially-coupled analysis is the thermal-stress analysis. It assumes that the stress/displacement in the mechanical model depends on the temperature history, but the temperature evolution in the part is independent of the stress/displacement fields. This assumption does not hold true in the presence of stress dependent thermal properties or large deformations, and a fully coupled analysis must be employed. According to the Abaqus documentation, the time history of temperature, electric potential, and normalized concentration are available for importing into subsequent stress, electrical, or mass diffusion analyses.

In the developed model in this study, the thermal analysis consists of temperature field calculation within the part as the laser beam moves through the powder and creates a small melt pool. As the laser moves away, the liquid metal cools down and solidifies. Afterwards, the time-dependent temperature profile is used as input to a mechanical analysis and thermal residual stresses are calculated. In the following sections, the details of each part of the analysis is elaborated.

3.1 Thermal Analysis

The three main heat transfer mechanisms, i.e. conduction, convection, and radiation can be considered in a thermal analysis in Abaqus. However, since radiation and convection are dependent on material properties and the surrounding environment, including them in the model needs to be based on experimental measurements of the powder absorptivity, the convective heat transfer coefficient, etc. This study, similar to [44, 39], neglected the direct consideration of the radiation and convection, and only considered the influence of conduction. The thermal material properties were taken from literature in this study. It is recommended to determine conduction (and possibly convection and radiation) properties through experiments.

3.1.1 Formulation

In Abaqus documentation [50], the general Green and Naghdi equation for energy balance is given as

$$\int_V \rho \dot{U} \, dV = \int_S q \, dS + \int_V r \, dV \tag{3.1}$$

where ρ is the material density; $\dot{U}$ is the time derivative of internal energy; q is the input heat flux per unit area; r is the amount of heat generation per unit volume; V and S are the volume and surface of a region of the body respectively.

The single direction dependency in sequential thermo-mechanical analysis can be described mathematically based on equation (3.1). This assumptions holds when internal energy is only a function of temperature ($U = U(T)$), and the none of the parameters ρ, q, and r are stress/displacement dependent. Otherwise, a fully coupled analysis must be employed.

The constitutive thermal model is expressed as:

$$c(T) = \frac{dU}{dT} \tag{3.2}$$

where c is the specific heat of the material. Again, for a sequentially coupled analysis, this parameter must not depend on stress/displacement.

The Fourier's law is used for heat conduction, which can be expressed as:

$$f = -k \frac{\partial T}{\partial x} \tag{3.3}$$

where f is the heat flux; k is the temperature dependent conductivity (which can be isotropic, anisotropic, or orthotropic); and x denotes position.

equation (3.1) in combination with equation (3.3), after spatial discretization takes the form of:

$$\int_V N^N \rho \dot{U} \, dV + \int_V \frac{\partial N^N}{\partial x} k \frac{\partial T}{\partial x} dV = \int_V N^N r \, dV + \int_{S_q} N^N q \, dS \tag{3.4}$$

where N^N functions are first- and second-order polynomials, which are used for temperature interpolation in one, two, or three dimensions.

For time integration, Abaqus uses the following form of time discretization:

$$\dot{U}_{t+\Delta t} = (U_{t+\Delta t} - U_t)(1/\Delta t) \tag{3.5}$$

which is the backwards difference method and is derived from the more general operator:

$$f_{t+\Delta t} = f_t + ((1-\gamma)\dot{f}_t + \gamma \dot{f}_{t+\Delta t})\Delta t \tag{3.6}$$

where γ is set to 1 (it is defined in the 0–1 range). This creates an unconditionally stable ($\gamma > 1/2$) solution without initial oscillations ($\gamma = 1/2$) according to the documentation.

Finally, by substituting the discretized form of $\dot{U}$ in equation (3.4) with equation (3.5), the result is:

$$\frac{1}{\Delta t} \int_V N^N \rho (U_{t+\Delta t} - U_t) \, dV + \int_V \frac{\partial N^N}{\partial x} k \frac{\partial T}{\partial x} dV - \int_V N^N r \, dV - \int_{S_q} N^N q \, dS = 0 \tag{3.7}$$

equation (3.7) is a non-linear system of equations which are solved using a modified Newton method.

3.1.2 Material Properties

Three properties pertinent to the considered heat transfer analysis are thermal conductivity, specific heat and density. For the sake of consistency, variety in material data sources was kept to a minimum. Thus these properties were taken from [28], because it had all three of them for temperatures up to 3000 K which is well beyond the melting point. In this reference the solidus and liquidus temperatures are both at 1700 K, thus the same was assumed for the finite element model in this study.

The conductivity has been plotted in figure 3.1 as a function of temperature. The dotted line shows the reference data and the solid lines represent the assumed material properties in this study. According to [28], the conductivity of liquid is less than that of solid. Several studies artificially increase the conductivity of liquid to account for convection heat flow in the liquid [51].

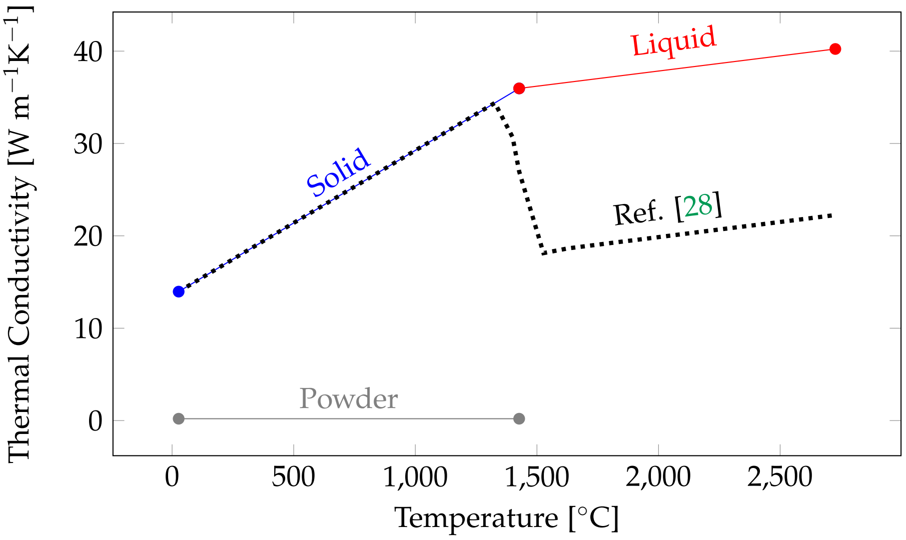

Figure 3.1: The considered thermal conductivity of different phases as a function of temperature in comparison with data from [28].

Similarly, this study shifted the liquid line upwards to follow the conductivity of solid, but with the increasing slope of the liquid phase. Towards the end of the project it became clear that the chosen conductivity for liquid metal underestimates the effect of convection. Thus the recommended value of 120 W m^{-1}K^{-1} from Goldak et al. [52] was used for the last simulation (section 4.5). Based on experimental measurements for steel 316 powder, the conductivity was around 0.2 W m^{-1}K^{-1} [53]. Thus it has been defined with a constant value.

In the reference [28], material properties were reported at 100 °C temperature steps. As the data points lied on a straight line, only two points were taken for each phase as shown in figure 3.1. For temperatures between points of definition, Abaqus interpolates the given data. If the temperature falls outside its range of definition, it uses the last value at the upper or lower bound.

The specific heat from ref. [28] and the three points which were used for its definition are shown in figure 3.2. In the experimental data, the specific heat of steel is constant after melting. However, in the FE model, the jump at the melting point was not included. An abrupt change in material data would make iterative calculations more difficult to converge. Therefore, it was assumed that the liquid specific heat increases gradually from the solid value at the melting point to 3000 K which is the maximum temperature given in the reference. For the solid and powder the chosen lines were the same as the experimental findings in [28].

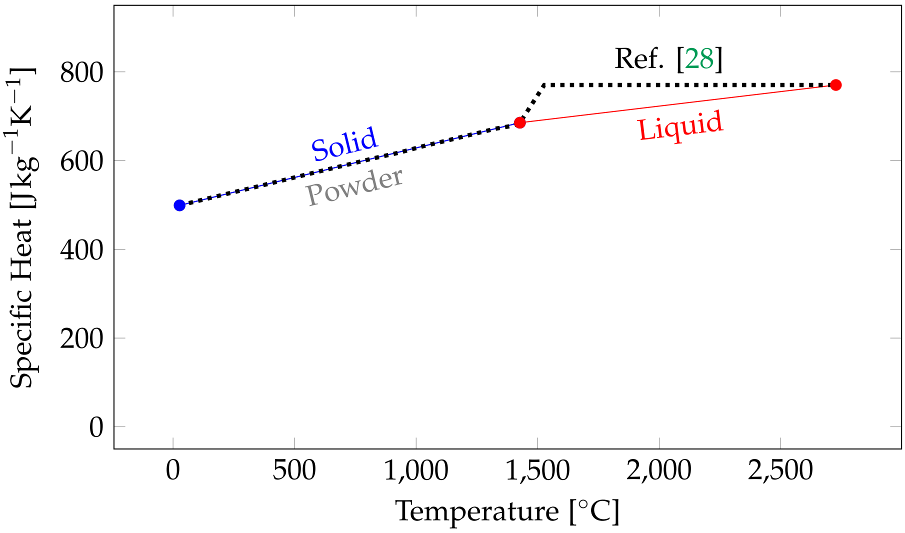

Figure 3.2: The considered specific heat of different phases as a function of temperature in comparison with data from [28].

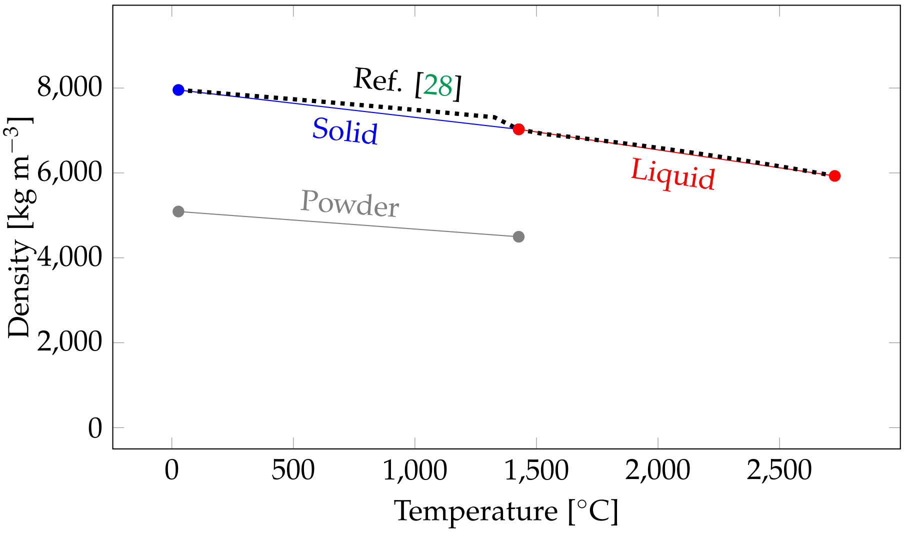

Figure 3.3: The considered density of different phases as a function of temperature in comparison with data from [28].

The density is illustrated in figure 3.3. The three points for the solid and liquid phase approximate the reference data quite closely. In case of powder, a porosity of 36% was assumed based on [53], thus its density is 64% of the solid phase.

Last but not least, air material properties were assigned to elements which were not active at certain time steps of the simulations. The thermal conductivity of air was set to zero. Otherwise, having a different volume of air above the layers would affect the temperature evolution. This assumption is valid since thermal conductivity and heat capacity of air are both 3 orders of magnitude smaller than metal.

3.1.3 Laser Definition

The laser beam is the main input to the system. It heats up the powder and causes the temperature increase and melting of metal. Residual stresses are dependent on the laser beam definition through thermal strains that develop in the part. As mentioned in section 2.2, the laser beam has a radius of 55µm. The laser distribution was chosen based on [54], where a Gaussian distribution perpendicular to the laser propagation direction and an exponential decay parallel to it is assumed:

$$Q = \frac{2AP}{\pi R^2 \delta} exp\left[-2\frac{(x-X_0)^2+(y-Y_0)^2}{R^2}\right] exp\left[-\frac{|z-Z_0|}{\delta}\right] \tag{3.8}$$

In this equation, Q is the body heat flux and is multiplied by element volume. A is the powder absorptance of laser, and P is the laser power. R is the laser spot radius, and is defined as the distance from center of laser where intensity falls to $1/e^2$ of its maximum value. δ is the optical penetration depth which is on the order of nanometers for bulk metals, but becomes much higher for powders where light beams can penetrate the gaps between powder grains. The first exponential term in equation (3.8) decreases the laser power in planes perpendicular to the laser propagation direction and the second one is for the intensity decay as laser penetrates the powder bed.

Table 3.1: Laser parameters used in the simulations.

Name	Abbreviation	Value
Laser Power (W)	P	100
Scan Speed (mm/s)	V	200
Powder Absorptance (%)	A	30
Spot Radius (µm)	R	55
Optical Penetration Depth (µm)	δ	60

The complexity of a moving volume heat flux with Gaussian distribution requires using the DFLUX subroutine in Abaqus. The code can be viewed in appendix A.1.

3.1.4 Phase Change and Layer Deposition

Once a powder layer is solidified, the next layer must be added for the process to continue. In Abaqus 6.14, adding elements during the simulation was not possible, and all of the elements had to be present in the simulation from the beginning. In order to reproduce the effect of element addition, air material properties were assigned to so-called inactive elements. Once the new layer is to be deposited, properties are switched to powder.

In order to assign different properties to elements based on time of the simulation, the material property definitions in Abaqus were dependent on a field variable. Any value can be assigned to field variables using the USDFLD user-defined subroutine. A sample-code is included in appendix A.2.

The second property-switch is the phase change due to melting. Powder, liquid, and solid have their respective properties for different temperature ranges and are distinguished through the same field variable used for element activation. However, the switch is temperature dependent in this case (as opposed to time-dependency in above case). The chosen representative values are shown in table 3.2.

Table 3.2: Representative values for each phase in the simulations.

Phase	FVD1
Air	0
Powder	1
Solid	2
Liquid	3

3.1.5 Thermal Boundary Conditions

For the temperature boundary conditions of the build, not much information was available at the start of the simulations. Two possible assumptions were insulation at all surface, or a temperature sink at the bottom of the substrate with room temperature. Since the heating process is very fast for short prints (on the order of milliseconds), an adiabatic assumption would not be far from reality. However, in cases where the printing process takes longer in many layers and multiples tracks, temperature increase due to the input heat would become too much and unrealistic. Therefore, a thermal sink at room temperature was assumed at the bottom of the substrate. For the final simulation a temperature history at approximately 5 mm blow the print area was available.

3.1.6 Mesh size and type

Since the laser radius was 55μm, the element size had to be smaller than that to capture the temperature gradients to a meaningful degree. On the other hand, decreasing mesh size, increases the number of elements by a power of three and significantly increases the computation time. A mesh size sensitivity analysis will be discussed in the next chapter. A 20μm × 20μm × 10μm element was chosen for the built part in the end. In the substrate, the height of the elements was increased linearly up to $1mm$ in order to reduce the computation time.

For heat transfer analysis, 8-node linear brick elements (DC3D8) were used. In the mechanical analysis the same mesh matrix was used, and only the element type was changed.

3.2 Mechanical Analysis

Once a thermal analysis is completed, its nodal temperature history can be used in a stress analysis to calculate the response of the system to thermal strains. In the mechanical model, the geometry, mesh matrix, and the heating and cooling durations are kept consistent with the thermal analysis. Only the material properties and the boundary conditions are changed.

3.2.1 Formulation

The mechanical simulations were performed using the "Static/General" step in Abaqus. According to the documentation [50], basic displacement problems are solved using the principal of virtual work:

$$\int_V \boldsymbol{\sigma} : \delta\boldsymbol{D}\, dV = \int_S \boldsymbol{t}^T.\delta\boldsymbol{v}\, dS + \int_V \boldsymbol{f}^T.\delta\boldsymbol{v}\, dV \tag{3.9}$$

where $\boldsymbol{\sigma}$ is the Cauchy stress matrix; $\boldsymbol{t}$ is the traction per unit are; $\boldsymbol{f}$ is the body force per unit volume; $\delta\boldsymbol{v}$ is the virtual velocity field; and $\delta\boldsymbol{D}$ is the virtual strain rate. After replacing the left hand side of equation (3.9) with its conjugate stress and strain pairing, it becomes:

$$\int_{V^0} \boldsymbol{\tau}^c : \delta\boldsymbol{\varepsilon}\, dV^0 = \int_S \boldsymbol{t}^T.\delta\boldsymbol{v}\, dS + \int_V \boldsymbol{f}^T.\delta\boldsymbol{v}\, dV \tag{3.10}$$

Similar to section 3.1.1 the interpolator functions are defined as:

$$\boldsymbol{u} = \boldsymbol{N}_N u^N \tag{3.11}$$

where u^N is any nodal variable. From kinematic compatibility between the displacement and virtual velocity field, a similar formulation can be used

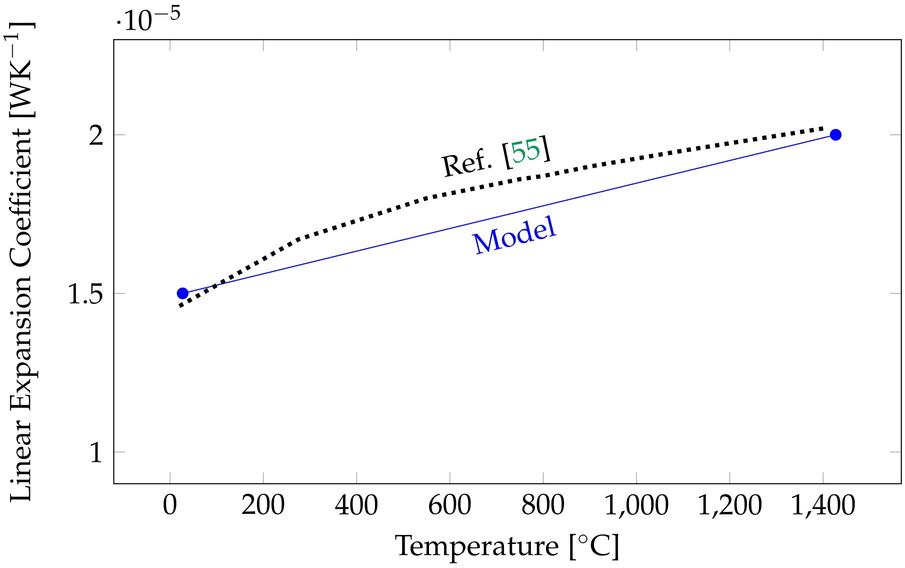

Figure 3.4: The considered thermal expansion coefficient as a function of temperature in comparison with data from [55].

for $\delta \boldsymbol{v}$:

$$\delta \boldsymbol{v} = \boldsymbol{N}_N \delta v^N \tag{3.12}$$

Lastly, for virtual strain rate $\boldsymbol{\varepsilon}$ the interpolation results in:

$$\delta \boldsymbol{\varepsilon} = \boldsymbol{\beta}_N \delta v^N \tag{3.13}$$

where $\boldsymbol{\beta}_N$ is derived from interpolations functions as the matrix of strain variations. By replacing above equations in equation (3.10), the following system of equations is reached:

$$\int_{V^0} \boldsymbol{\beta}_N : \boldsymbol{\tau}^C \, dV^0 = \int_S \boldsymbol{N}_N^T . \boldsymbol{t} \, dS + \int_V \boldsymbol{N}_N^T . \boldsymbol{f} \, dV \tag{3.14}$$

Which can be solved for the stress and displacement field. Further details can be found in the theory section of Abaqus documentation.

3.2.2 Constitutive Model

The property that ties thermal/mechanical analysis is the thermal expansion coefficient which changes from 1.5×10^{-5} at room temperature to 2^{-5} at the melting point [55] (figure 3.4).

The elasticity modulus for stainless steel has been taken form [55]. In the solid phase, elasticity has been approximated with two solid lines and the

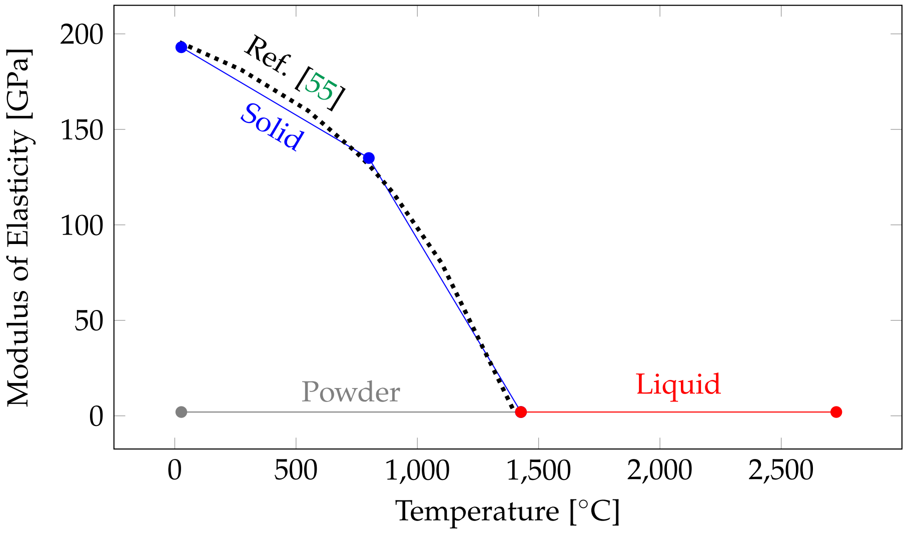

Figure 3.5: The considered modulus of elasticity for different phases as a function of temperature in comparison with data from [55].

powder/liquid were assigned one percent of the value for solid at room temperature according to recommendation by [56].

In order to capture residual stress development in the part, it is necessary to employ a plasticity definition in the material model. Therefore, isotropic hardening was chosen for the plastic behavior based on [57]. The employed data in this study can be seen in figure 3.6. Mullins et al. [57] have reported a peculiar behavior for the yield strength of stainless steel 316. In their hardening plots, yield strength decreases by increasing temperature up to 600 °C, but shows a sharp increase at 700 °C and continues to decrease at higher temperatures. This phenomenon is referred to as *dynamic strain aging* [57] and its influence on development of thermal stress is discussed in section 4.2.3.

As described in the next chapter, hardening definition alone without any sort of annealing due to high temperatures exposure would result in unrealistically high residual stresses. When the elements are in liquid phase in the simulations, the equivalent accumulated plastic strain keeps increasing. In practice, this variable does not hold meaning in the liquid phase. The large accumulated plastic strain forces the software to assume large yield stresses based on figure 3.6. In order to avoid that, the strain hardening memory is cleared due to annealing.

Annealing is a complex phenomenon that happens even at much lower temperatures than the melting point (for instance 750°C [58]). However, as no data regarding its precise definition was available, the recommendation by

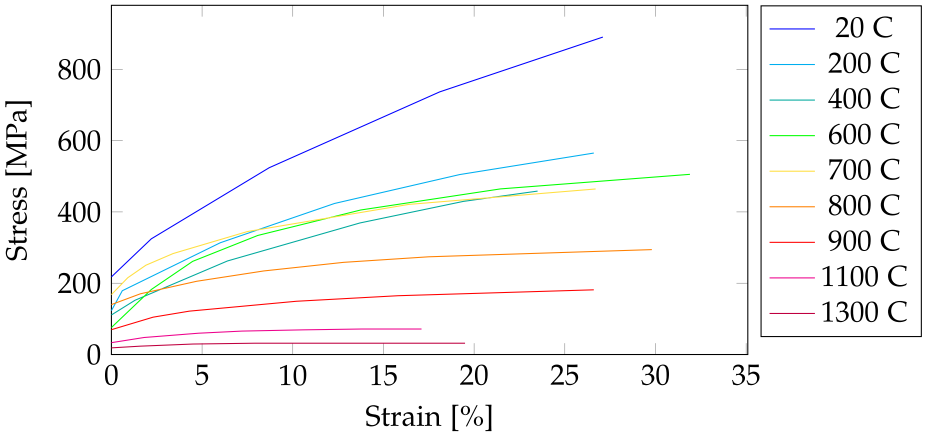

Figure 3.6: Stress-strain behavior of stainless steel 316 beyond the yield point at different temperatures [57]

the same source for hardening data [57] was used and an annealing temperature of 1400 °C was assumed (the melting point is taken as 1427 °C in comparison). Beyond this temperature the accumulated plastic strain is set to zero and when the solid cools down it starts on the hardening curve from zero strain.

3.2.3 Mechanical Boundary Conditions

Manufactured parts with SLM are clamped to the substrate, but setting the node displacements on the bottom surface to zero in Abaqus would impose unrealistic stresses. Therefore, in order to restrain free translation and rotation of the part in the simulation, the bottom surface which was in the form of a rectangle was fixed perpendicular to its surface. In order to stop free movement in the same plane, two non-parallel sides of the rectangle were constricted perpendicular to their direction.

3.3 Miscellaneous

In this section, some of the issues with the development of finite element code that do not fall under other topics are discussed.

In Abaqus, the node locations in the input file are stored with 8 significant figures but the values are not truncated. This caused problems in the DFLUX subroutine as the exact coordinates of the nodes were used to define the boundary of the heated volume. Wherever this small difference caused the node to fall out of the assigned boundaries, there was less heating and thus lower temperatures. This problem was solved by rounding nodal coordinates up to 8 figures. Another solution is including a small margin in the boundary of heated volume to make sure all target nodes were included in the laser definition. Alternatively, one can define element sets beforehand for regions of interest in the subroutine, and avoid using exact coordinates for setting the boundaries.

Another issue with the DFLUX subroutine was how the element volume was defined and assigned to each node. Through numerous trials it became clear that in brick elements, the representative volume for a node is the sum of 1/8th of the volume of its surrounding elements. If the node lies on the outer surface of the geometry, only half of the element volume would be assigned to it. This significantly reduced the amount of laser energy input where it moved on the outer surfaces. In order to fix this problem, an extra layer of inactive elements is always included in the model, and the laser was never applied to surface nodes.

Chapter 4

Results and Discussion

4.1 Reference Model

After multiple iterations and testing out various assumptions, a model was created which followed basic physical principles and generated satisfactory results both in thermal and mechanical domain. Since the sensitivity of simulations to different variables are investigated with respect to this model in section 4.2, it is referred to as the *reference model*. In the following, a description of general aspects of it is discussed.

4.1.1 Attributes

Geometry

10 layers of powder were printed. In each layer, the laser beam followed a single track of 1 mm length. The melt pool was 100 µm in width and the total thickness of the model was 300µm. i.e. an extra 100µm thick powder layer was around the printed area. Underneath the printed layers, a solid substrate with a rectangular cross section of 100µm × 1mm and 1 mm height was included to support the newly formed solid elements.

Step Definition

For each layer, two steps were defined. In the first one, laser source was active and the complex thermal/mechanical interactions occur. Once the print is finished, it is left to cool down for roughly 1 second in the second step. Afterwards, the subsequent layers are printed in the same manner until the job is finished. Duration of heating steps depends on laser speed and the track length. In this case, with 200 mm/s speed and 1 mm track length, it takes 5 ms. Finally, the maximum temperature change in each increment is set to 500 °C since the heating process is quick and temperature changes are

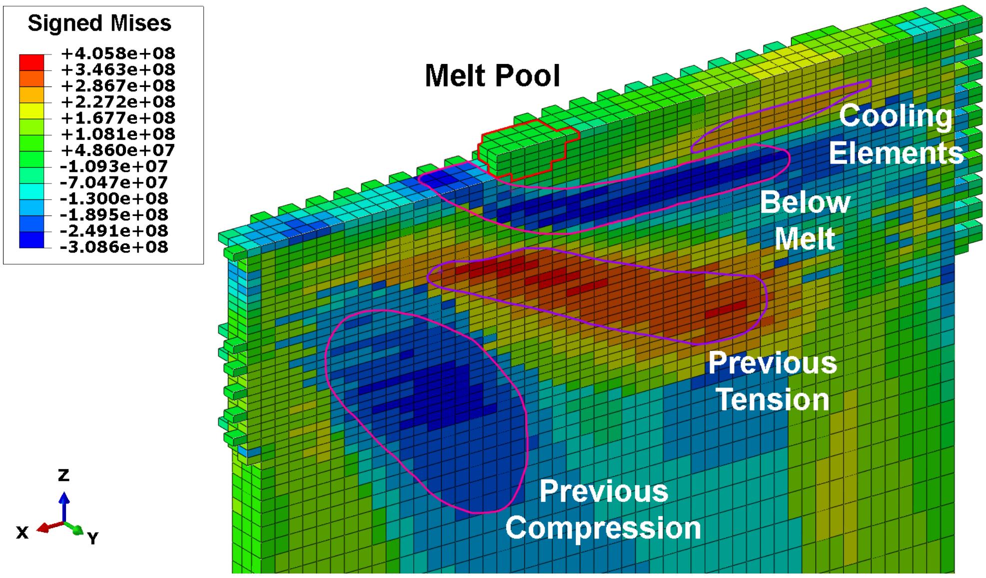

Figure 4.1: Signed mises distribution during printing of the 10th track.

large. Setting this value lower can help when there are convergence issues but does not significantly change the final result .

4.1.2 Stress Evolution

Figure 4.1 is the cross section view of stress distribution during printing of the last layer. The illustrated parameter is *signed mises*, i.e. the von Mises stress multiplied by sign of the hydrostatic stress (negative of the pressure). The positive sign indicates that the element is under tension, while negative signifies compression. In this figure, the excess powder is excluded and only the solid/liquid elements are shown.

The elements inside the red outline are in the liquid phase. They appear as green because the liquid phase is assumed to be stress free. The area just below the melt pool falls under compression because of the temperature increase ensuing thermal expansion. The previously melted elements fall under tension as they cool down and shrink due to constraints from surrounding volume. Further below the melt pool, tensile and compressive areas are seen which have developed in previous prints and are still affected by the melt development in the top layer.

In figure 4.2 the stress distribution at the end of the process is shown. The maximum tensile stress occurs not directly in the top layer, but a few layers below. In response to the tensile region, a compressive stresses can be seen below it.

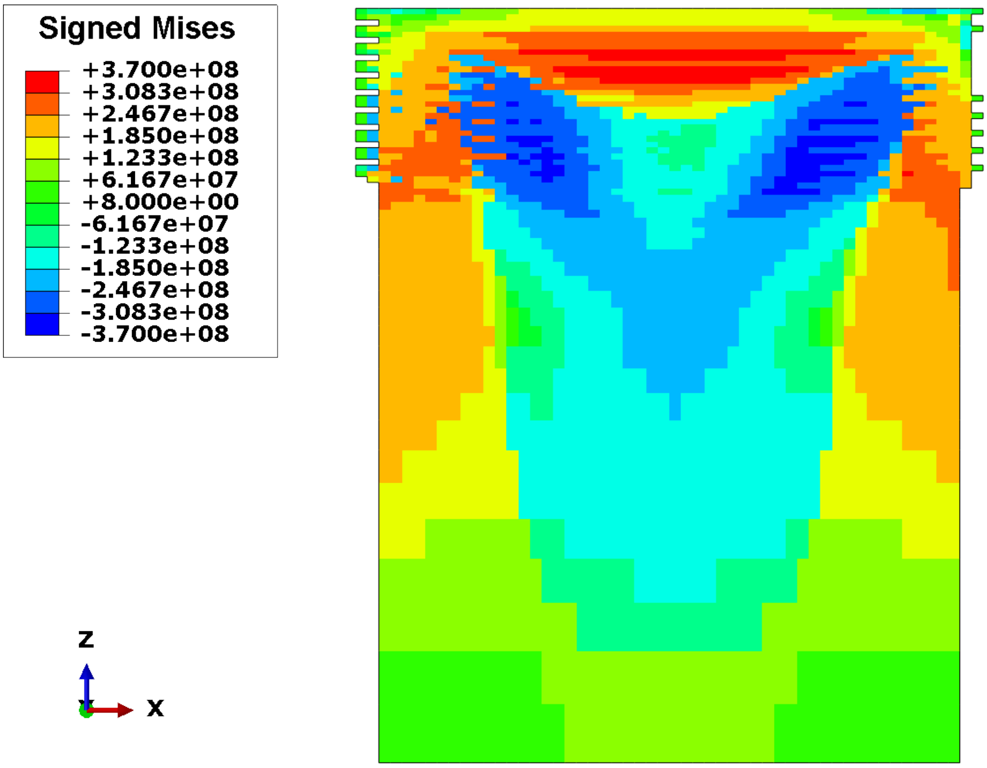

Figure 4.2: Signed Mises stress distribution after print of the 10th layer and final cooldown.

In the next section, sensitivity of the developed residual stresses in the reference model to changes in different parameters and assumptions is discussed. First, a mesh sensitivity analysis is presented to show how the output results (temperatures and stresses), and computation time change with decreasing element size. Then, the effect of using multiple integration points in an element instead of one, is investigated. Afterwards, the question of whether a fully coupled analysis would be necessary or not is explored. Next, the effects of a large solid substrate (instead of the thin substrate described in section 4.1.1) on residual stress development is presented. Lastly, two assumptions regarding the constitutive model are turned off, and the resulting changes are discussed.

4.2 Sensitivity Analysis

During finite element model development, assumptions had to be made at different stages in order to reach a physically sensible model that could be solved in a reasonable time. In this section, these assumptions are investigated one at a time, and the changes in the output results (residual stresses

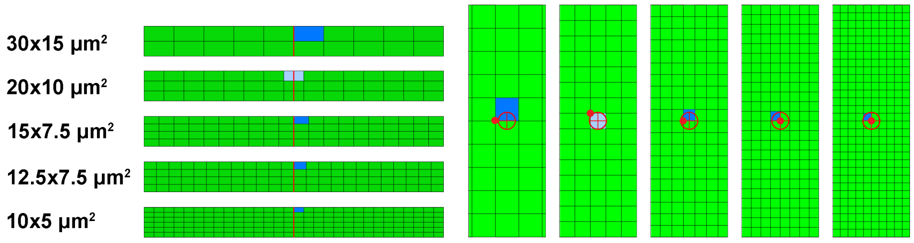

(a) Side view (b) Top view

Figure 4.3: a) Cross-section side view at the middle of the first layer. b) Top view at the middle of the first layer.

and temperature fields) are discussed.

4.2.1 Mesh Size

A inherent part of any simulation is choosing an optimum mesh size for the model geometry which can satisfy two qualities.

- Further reduction of the mesh size should not change the output result beyond a certain margin of error.
- The calculations should be computationally as least expensive as possible.

Usually a large mesh size is adopted in the beginning and is reduced in size until the accuracy criteria is satisfied. The geometry considered for the mesh size analysis was similar to the reference model but with only 2 layers instead of 10 in order to cut down on simulation time.

In figure 4.3 the different mesh patterns are illustrated. figure 4.3a is the cross section of the first layer. The red line in the middle shows the location of the laser at the time frame that the temperature was recorded. The elements highlighted in blue are where the mises stress at the end of the simulation was used for comparison (light blue is the mesh size which was used in the simulations eventually). In figure 4.3b the same location but from the top is shown. The blue element is the same as before, and the red reticle shows the laser position. Finally the nodes under the red dot are the closest to the laser location, and their temperatures were analyzed for comparison.

For measuring the effect of changing the element size on simulation results, maximum nodal temperature from the thermal analysis and the final von-Mises stress from the mechanical one were chosen. The changes in these parameters with increasing number of elements is shown in figure 4.4.

For the subsequent simulations, and the one mentioned in the previous section, the second largest element size was used. In figure 4.4, with changing

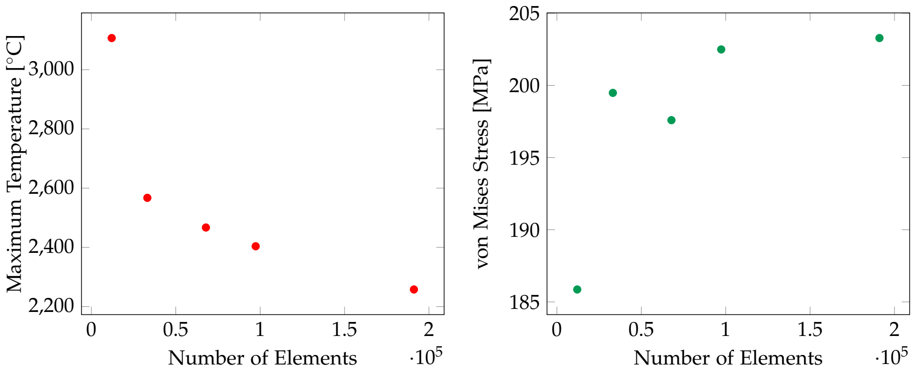

(a) (b)

Figure 4.4: Mesh size effects on simulation results. a) Maximum nodal temperature decreases with increasing number of elements. b) The final residual stresses decrease with smaller element size.

the mesh size from 30µm to 20µm, the temperature drops by 7.3%, while the relative changes in the next three reductions are 0.9%, 2.5%, and 0.39%. Furthermore, there is a 17.3% drop in the residual stresses with the first mesh size reduction while lowering it further results in 3.9%, 2.5%, and 6.1% relative variations. Therefore, the reasoning behind choosing this mesh size was that using smaller element size did not change the results in a deterministic manner. With this element size, there is an uncertainty of ±2.5%, and ±6% in temperature and residual stresses respectively.

The second factor in choosing the mesh size was the calculation time, which is shown in figure 4.5. Reducing mesh size increases the number of elements by a power of three which itself increases simulation time respectively. For instance, if each dimension of the reference element size (20µm × 20µm × 10µm) is divided by 2 (10µm × 10µm × 5µm), the number of elements increases by a factor of 8, and simulations take 16.3 times longer. It should be noted that the times discussed here are for printing only 2 layers with a single 1 mm track. The conducted simulation with the chosen mesh size in the reference model took around 20 hours. Thus smaller elements would have been impractical, and calculation time was the limiting factor in choosing the mesh size.

4.2.2 Fully Integrated Elements

For the mechanical analysis, linear brick elements were used (figure 4.6). In Abaqus [50], there are two types of such elements based on the number of integration points. The fully integrated element has 8 integration points and is denoted by C3D8, while the reduced version has only 1 integration point

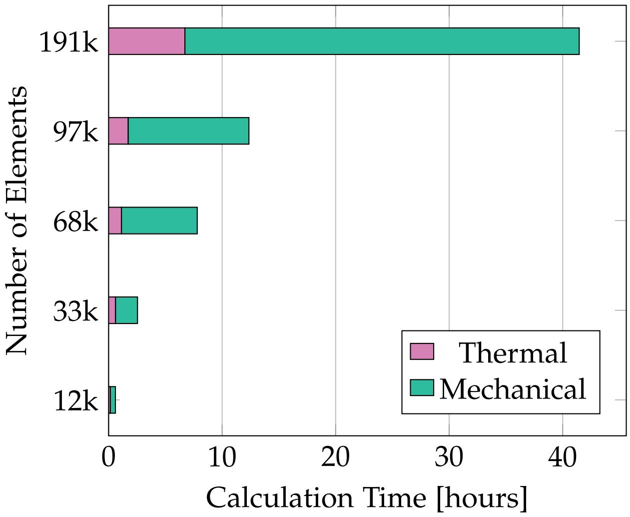

Figure 4.5: Comparison of calculation time for different mesh sizes in printing two layers for thermal and mechanical analyses.

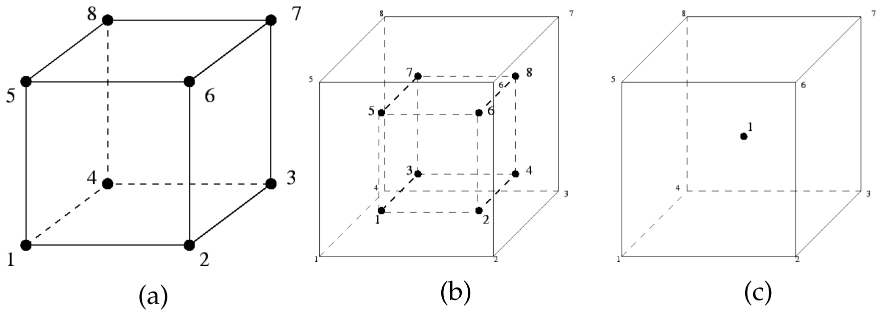

Figure 4.6: C3D8 and C3D8R element nodes and integration points. a) Location and numbering of nodes. b) Position of integration points in the fully integrated element. c) There is only one integration point in the reduced element. [59]

in the middle and is differentiated from the former by an R at the end of element name (C3D8R). The first impression of a fully integrated element is higher calculation time. While this is true, it is not the only difference between the two types. Each of them has advantages and disadvantages which should be considered carefully before choosing one of them for mechanical simulations.

In the Abaqus documentation [50], it is explained a major issue with fully integrated elements is *shear locking*. It refers to development of so-called parasitic shear strains that do not exist. Shear locking usually occurs in long and slender structures that are subject to bending. Since 8 node elements

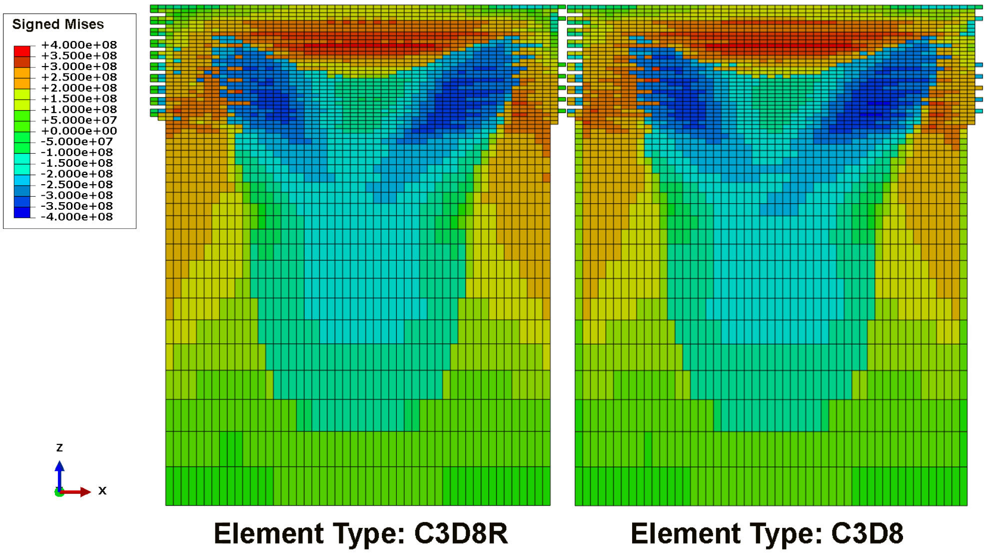

Figure 4.7: Comparison of residual stresses with two element types.

do not bend, the deformations take the form of shear strain as the elements are compressed on one side and stretched on the other side. This results in high shear stresses and increases the overall stiffness of structures, thus the term: shear *locking*. In our simulations bending is not the primary mode of deformation, but in order to reduce calculation time, fully integrated elements were avoided.

The reduced integrated elements are not without issues either. Hourglassing can happen with these elements, which refers to a type of distortion where the calculated strains at the single integration point are zero. Abaqus includes hourglass control to mitigate these effects. Nonetheless, it is recommended to use a fine mesh with reduced integration elements and distribute localized loads/boundary conditions over a number of elements [50].

The reference model was solved with both element types and the stress distribution in z-x cross section view can be compared in figure 4.7. Since no major differences were observed, the reduced element type was chosen for the rest of the simulations due to its less complexity and better performance time-wise.

4.2.3 Fully Coupled Analysis

As mentioned in chapter 3, sequentially coupled thermal-stress analysis was used in order to reduce simulation time. In this section, the effects of mechanical deformations on the thermal field are investigated.

Similar to mesh sensitivity, 2 layers with a 1 mm laser track length were

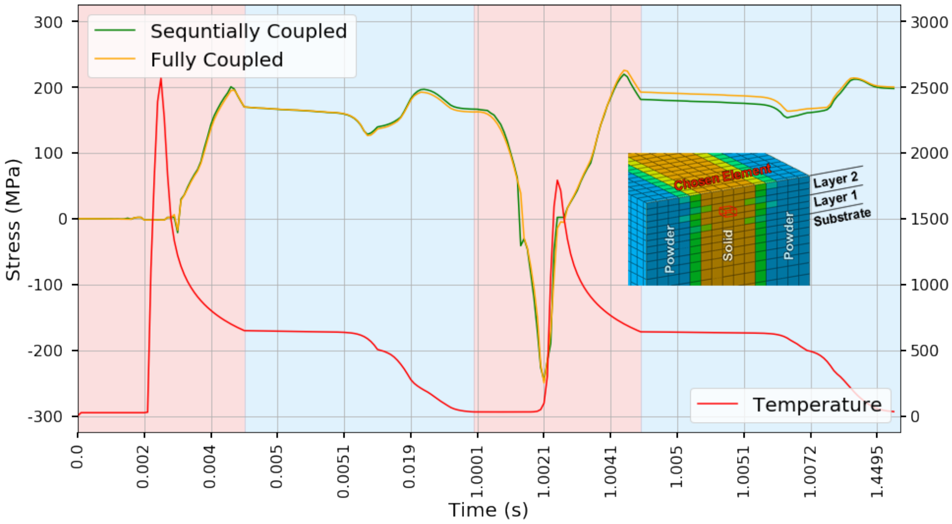

Figure 4.8: von-Mises stress evolution during print process (at the shown element in the inset) in sequentially vs. fully coupled analysis.

used for this analysis. In figure 4.8, the signed mises stress evolution for the middle element on top of layer 1 is shown. The areas highlighted in red show the heating step while those in blue correspond to cool down time. On the second axis the temperature history in one of the nodes of the element is shown. It can be seen that the stress becomes nearly zero when the temperature rises above the melting point ($T_{melt} = 1427°C$).

The general purpose of figure 4.8 is to show that not only the final value of stress, but also its time history is similar in both fully and sequentially coupled analyses. In addition, interesting information about the behavior of the hardening model discussed in section 3.2.2 can be inferred from the figure.

In the beginning, the element is in powder phase and free of stress. As the temperature increases above the melting point, it turns to liquid. Between the 2 ms and 4 ms windows, the signed Mises stress becomes negative. This compression is due to expansion of its surrounding elements as the laser moves close to the element. Beyond the melting point, the element changes to liquid phase but still the stresses are low. The cooling of the element starts immediately after the laser moves away from it. As cool-down continues, the element turns to solid and larger stresses start to build up. At around 700 °C the stress levels start to fall. This phenomenon is due to the dynamic strain aging which was mentioned in section 3.2.2. Stress keeps going down in the cooling step until the temperature falls below 600 °C. In the material model, yield strength increases by decreasing temperature below 600 °C. Thus the residual stress becomes larger as well. In the second heating phase, the effect

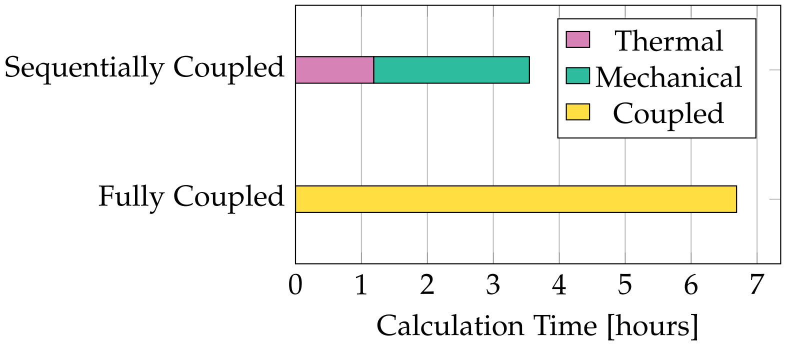

Figure 4.9: Calculations time in fully and sequentially coupled thermal-stress analyses.

of compression due to expansion of the top layer is more evident.

The calculation time for the two simulations is compared in figure 4.9. Fully coupled analysis takes almost twice as long as its sequential counterpart. This is another advantage of separating the thermal and mechanical aspects of the problem.

4.2.4 Large Solid Substrate

In figure 4.10, the stress distribution in a model with a large solid substrate is compared with the reference model. The deformations are scaled 5 times for better illustration. In the corners, where the print is attached to the substrates the elements appear as gray, meaning that the stresses at these locations is very high and as seen on the legend, they can be up to 731 MPa. This is due to stress concentration which increases as additional layers are printed. In samples produces by Tolosa et al. [10], cracking and delamination at the bottom of some SLMed parts was seen due to the same phenomenon.

In the left hand side, the same area is free to deform and does not carry such high stresses. Since this sort of localized stress was not wanted in other sensitivity analyses, the thin substrate was adopted.

4.2.5 Constitutive Model Assumptions

Development of residual stresses in finite element simulations is directly dependent on the constitutive material model definition. A description of the employed isotropic hardening plasticity model has already been given in section 3.2.2. In the following, the effect of two assumptions on the final developed residual stress distribution is investigated.

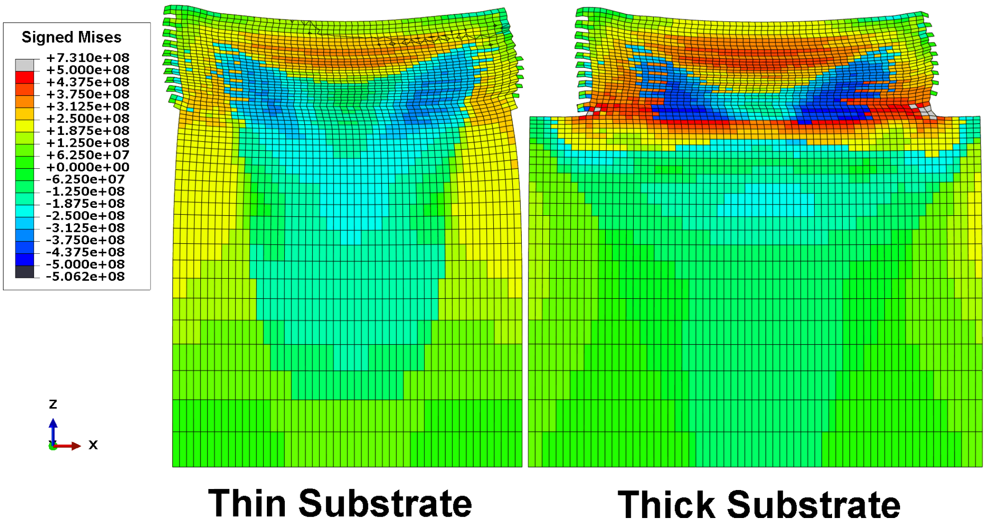

Figure 4.10: Stress distribution with a thick solid substrate. The deformation are shown with a ×5 scale.

Perfectly Plastic Model

Along the stages of finite element model development before reaching the final set of assumptions, there was no hardening included in the plasticity definition, and only a perfectly plastic solid was present. In figure 4.11 the final singed mises distribution in x-z cross-section is compared for the two cases. As expected, the stress levels are much lower in the perfectly plastic case. Maximum tensile stress in the reference model reaches up to 360 MPa while in the other case, it does not surpass 200 MPa. This shows that the residual stresses are highly sensitive to the hardening definition. It is recommended to conduct tests on SLM parts themselves, and derive the relevant constitutive model for simulations.

Annealing Temperature

As mentioned in section 3.2.2, annealing is an import part of the hardening model which must be included in the finite element simulation. In this section the consequence of having no such property on the residual stress development is investigated. Figure 4.12 shows the signed mises distribution in z-x cross section of the 10-layer print, in the two cases. As seen on the right hand side, the stresses can rise up to 600 MPa if the effect of temperature rise on reseting hardening is ignored. In order to avoid this unrealistic outcome, the anneal temperature of 1400°C was adopted even though it is not a direct physical representation.

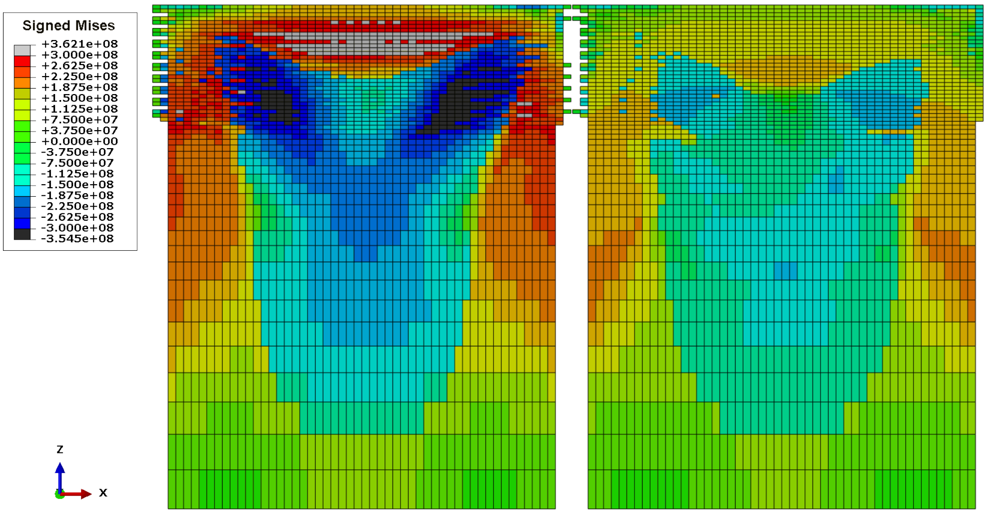

Isotropic Hardening **Perfectly Plastic**

Figure 4.11: The signed mises stress distribution with perfectly plasticity compared to the reference model.

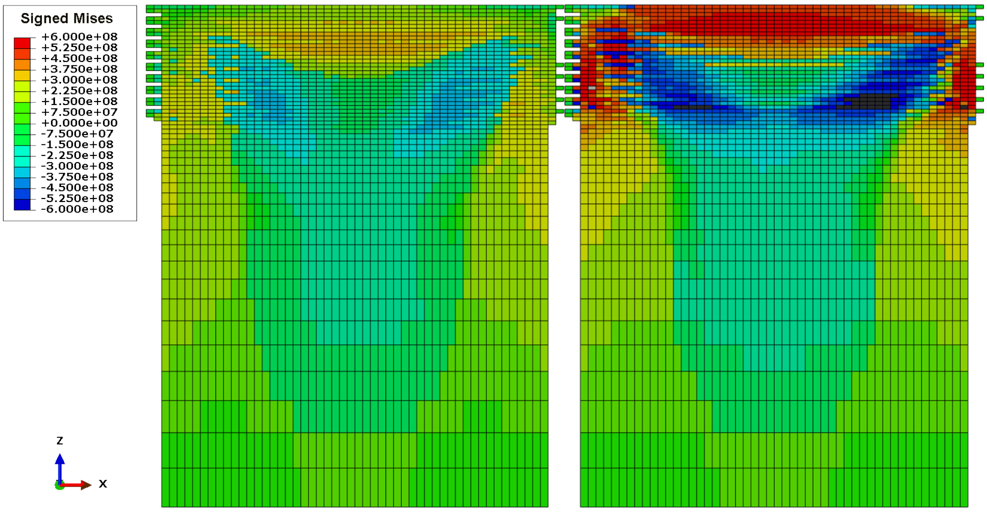

Anneal Temperature = 1400 **No Anneal Definition**

Figure 4.12: The signed mises stress distribution without annealing temperature definition compared to the reference model.

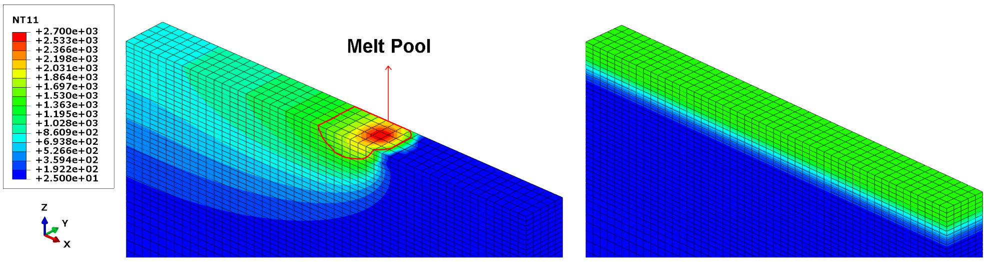

Figure 4.13: Temperature distribution in the reference model compared to liquid deposition in the simplified approach.

4.3 Simplified Model

An all-inclusive model would be great for predicting thermo-mechanical response of parts with respect to different variables, but the increased complexity results in long calculations. Therefore, for the goal of modeling real world parts, even more simplifying assumptions need to be made.

The major constriction on increasing element size is the laser spot diameter. The small size of it requires even smaller elements in order to capture a meaningful temperature distribution. In previous works [42] heating the whole layer to a certain temperature has been done instead of a moving laser as a way of simplification. In order to investigate how this could affect the stress distribution, the same was done for the 10-layer reference model with a slight modification. The extra powder which was mentioned previously was excluded from the model and only the solidifying elements were present.

At the start of each heating step, a layer of liquid metal at the melting point was deposited and held at the same temperature for the same duration as laser would have passed through i.e. 5 milliseconds (figure 4.13). The resulting stress field is shown in figure 4.14. The distribution is very similar and there is only a 6% change in the maximum tensile stress in the part.

Calculation time can be compared in figure 4.15. The simple model takes less than an hour while having full laser definition causes a five-fold increase in simulation time. It should be noted that, for the sake of comparison, the same mesh matrix was used for the simplified model whereas with absence of laser definition, one can increase element size and reduce computation time even further. Such a decrease in calculation time, in addition to the small changes in stress distribution show promise for using simplified models for real world sized parts.

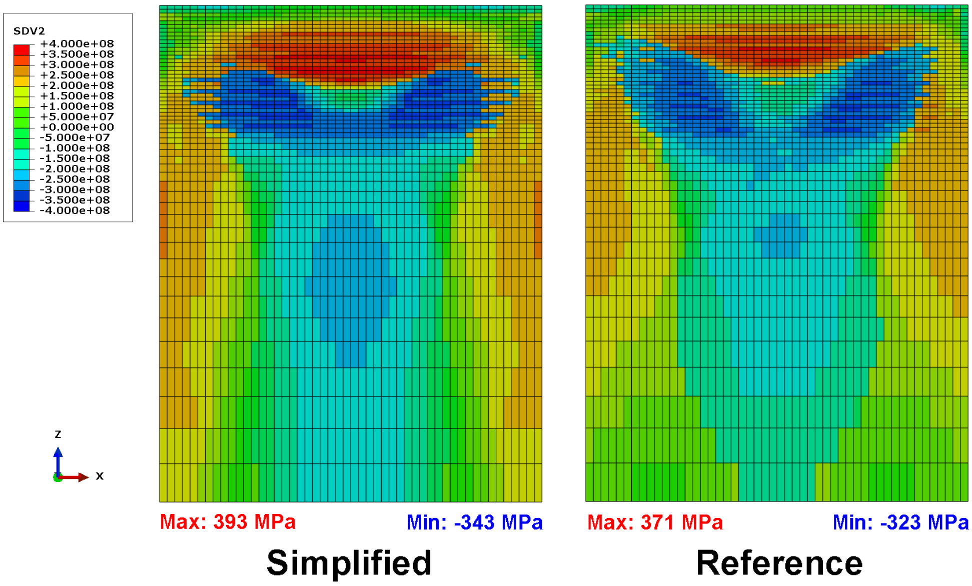

Figure 4.14: The signed mises stress distribution in the simplified model and the reference one.

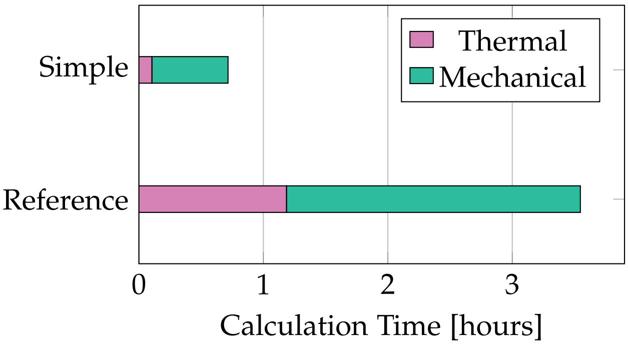

Figure 4.15: Comparison of calculation time for the simplified model vs. the reference one.

4.4 Parametric Study

In section 4.2, the effect of different model assumptions on the output results was investigated and a final model was decided upon, which was discussed initially in section 4.1. At this stage, it is of interest to know how this model would respond to changes in process parameters. In the following, the laser power, scan speed, hatch space, and preheat temperature are varied and their effects on the output results are investigated. As a form of model validation, the results are compared with similar experimental parametric studies [35].

Up until now, the models mainly consisted of 1 mm single laser tracks up to 10 layers, which does not show the effect of side by side prints. Thus for this section, another geometry with 3 layers, each with 3 laser tracks of 1 mm length (9 mm total scan length) was used.

4.4.1 Laser Power and Scan Speed

Some of the process parameters that directly control the quality of the print and can be chosen by the operator are the laser power, scan speed, hatch space and layer thickness. The combination of these four qualities determines how much energy is given to system per unit volume. In other words, the energy density depends on these variables. Therefore, changing only one of them can result in egregious issues such as unmelted powder or vaporization. In order to compare the effect of changes in these parameters, we held the ratio of laser power to scan speed constant, and changed them in pairs as in table 4.1.

Table 4.1: Pairs of laser power and scan speed with constant ratio.

1 mm Scan Time (ms)	4	4.5	5	5.5	6
Laser Power (W)	125	111.1	100	90.9	83.3
Scan Speed (mm/s)	250	222.2	200	181.8	166.6

Choosing a single element for comparison was quite difficult because both the stress distribution and values changed in each case. For instance, the region of highest tensile stress was not at the same exact elements. Additionally, the highest tensile element changed in location and value without a clear pattern which could be due to discretization errors. Comparing the cross-section view as was done for the 10-layer single track models was not as useful, since there are only 3 layers in this model. Therefore, in order to capture both the distribution and stress values in a single parameter for the

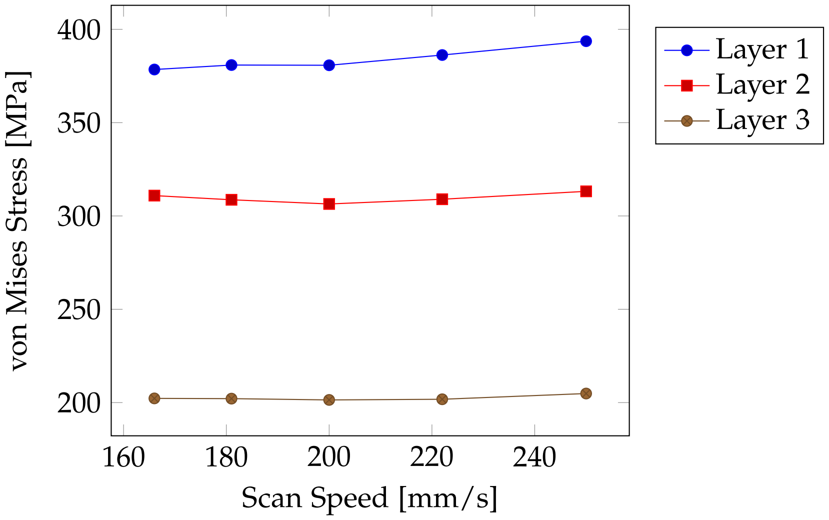

Figure 4.16: Average of developed residual stresses during SLM in three layers with different scan speed/laser power combinations.

sake of comparison, the average residual stress in each of the three layers was measured.

The average von-Mises stress in the solidified part of the three layers is shown in figure 4.16. A similar parameter study on SLM of steel 316 was done by Shiomi et al. [35], which is used in assessing these results. They changed the scan speed in 4-8 mm/s range and the tensile residual stresses remained in the 300-400 MPa region. This behavior can be seen in figure 4.16 too where there is negligible increase in the residual stresses with increasing scan speed. Therefore, one can conclude that as long as an stable melt pool forms, residual stresses are independent of the scan speed (otherwise balling, keyhole formation or increased porosity happen which are not considered in this finite element model).

4.4.2 Hatch Spacing

Using 3 laser tracks in each layer enabled investigation of hatch space effect on the residual stresses. In figure 4.17, the average layer stress is plotted for 40 µm, 60µm, 80µm, and 100µm values of hatch distance. As the melt pool overlap decreases, some of the powder is left unmelted between the solidified regions which greatly decreases residual stresses. In practice, in porous media the stress perpendicular to the free surfaces inside the material would be zero. On the other hand, decreasing hatch space, increases the residual stresses. The reason for this behavior can be due to so-called *double quenching* in the overlap region which becomes larger with smaller hatch space [60].

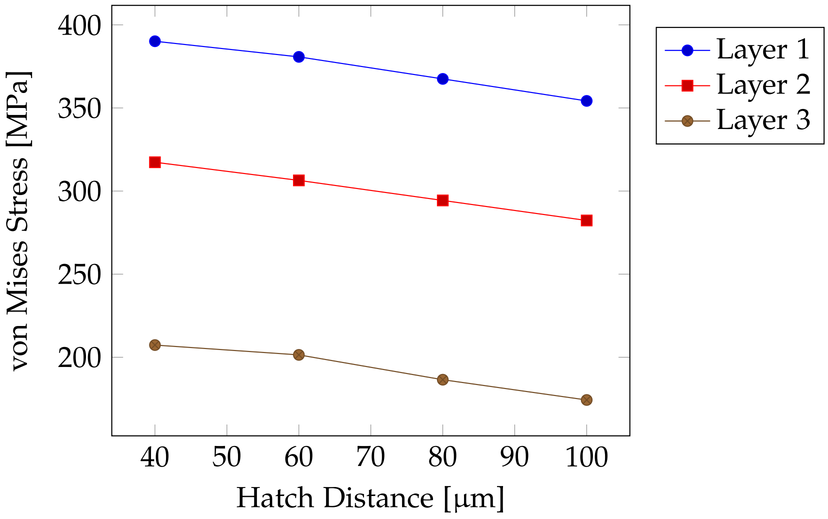

Figure 4.17: Mean value of developed residual stresses during SLM over the three layers with different hatch spacing.

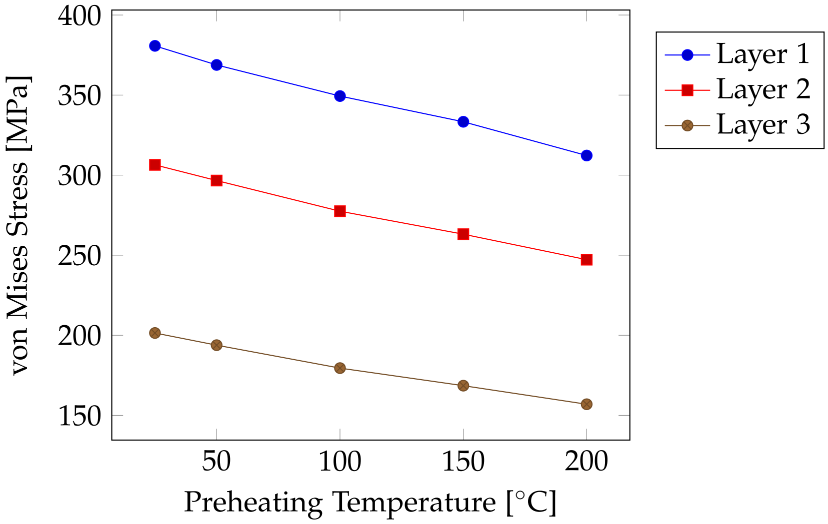

Figure 4.18: Average value of SLM residual stresses in the three layers with different substrate preheating temperatures.

4.4.3 Preheating

In some SLM machines it is possible to preheat the substrate to a certain temperature in order to decrease the residual stress levels in the manufactured part. The results of increasing substrate temperature can be seen in figure 4.18. This decrease in the residual stresses has also been confirmed by Shiomi et al. [35].

4.5 Model Verification

In this section, the result of a simulation similar to the experiment of chapter 2 is presented. The laser parameters of the experiment were slightly different from table 3.1. The scan speed was 800 mm/s and the laser power was 150 W. This resulted in a smaller laser power density than what had been used previously in the simulations, which created a smaller melt pool. Upon further investigation it became clear that the chosen powder absorptance was lower than what it would have been in the experiment. According to Trapp et al. [61], for the given laser power and scan speed, the heat transfers through the keyhole mode. In other words, metal vapor bubbles form and the melt pool would be deeper than the conduction mode heat transfer. Under these conditions, the absorptance of steel 316 powder rises up to 80%.

In the simulations, the liquid flow, vaporization, surface tension, wetting, and most phenomena related to molten metal was neglected. As a form of compensation, the exponential decay of laser with depth inside the powder bed was removed (in order deliver more heat to the bottom of the layer as happens with wetting). Additionally, an arbitrary value of 40% was chosen for absorptance.

Table 4.2: Laser parameters of the experiment which were adopted for the final simulation.

Name	Abbreviation	Value
Laser Power (W)	P	150
Scan Speed (mm/s)	V	800
Powder Absorptance (%)	A	40
Spot Radius (µm)	R	55
Optical Penetration Depth (µm)	δ	30

For making a comparison between the simulations and experimental data, the exact position of the thermocouples on the thin wall structures was needed. In order to find these spots, the blades were painted black and then, the wires were removed. This caused the weld spots to appear as bright spot among the black paint under the microscope. One such image is shown for ET3 thermocouple in figure 4.19.

As discussed in section 2.3, due to mounting misalignment, the temperatures at two sides of the same structures were different. Since this problem was more pronounced in the first and second structures, the simulation is only compared with the third one (closest to the center of the substrate). The results are shown in figure 4.20.

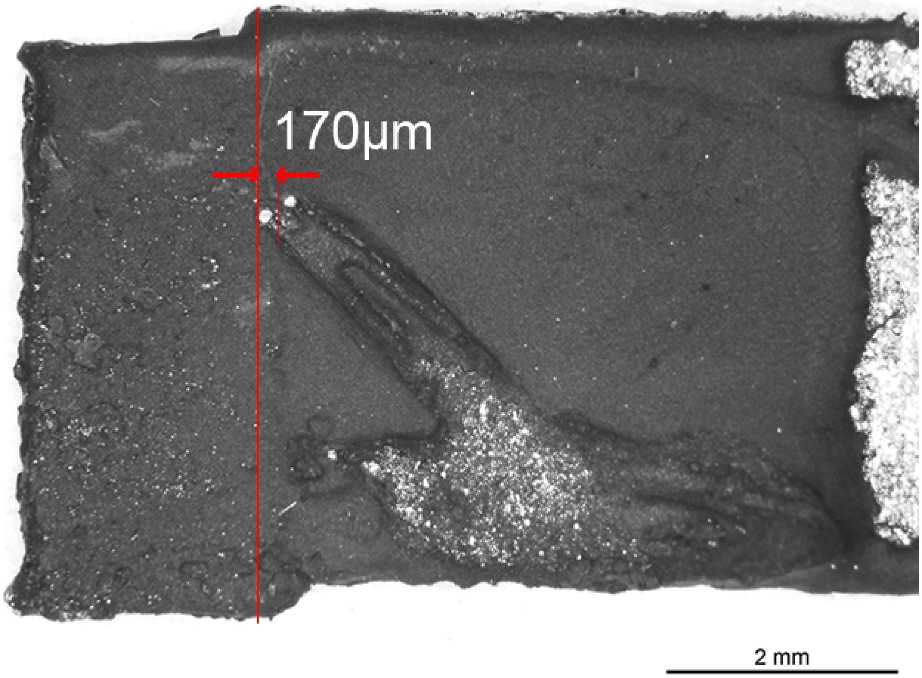

Figure 4.19: Colored thin wall after detachment of thermocouples. Bright spots correspond to previously attached wires.

The maximum temperature is predicted closely, but during cool-down the simulation temperatures are higher. This might be due to a higher conductivity of the material in the experiment. Additionally, the neglected heat transfer mechanisms such as convection would contribute to faster heat dissipation and lower temperatures which were not considered in this model.

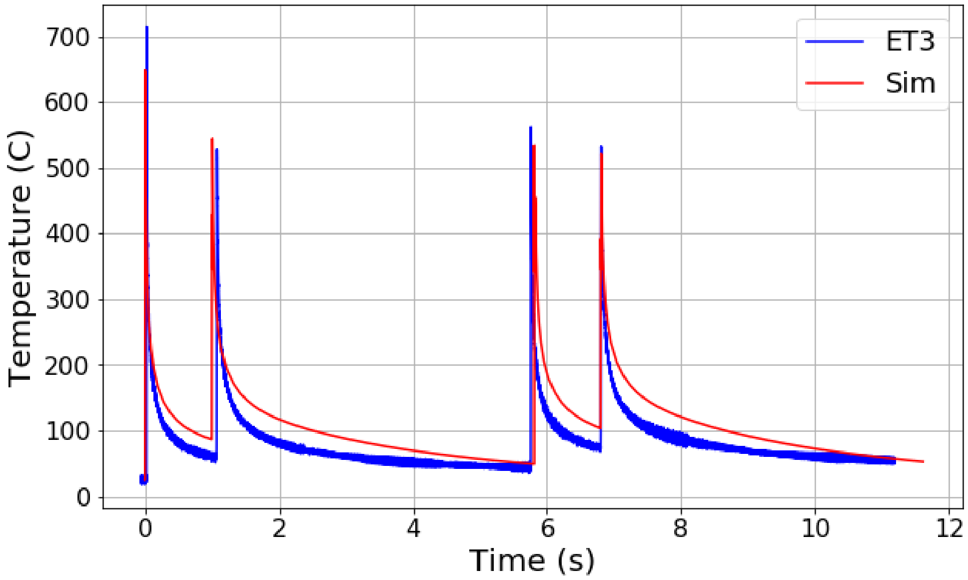

Figure 4.20: Temperature history on top of the substrate during printing of the first two layers in the third thin wall and the corresponding simulation.

Chapter 5

Summary and Outlook

5.1 Summary

In this work, thermal history and residual stress development during selective laser melting process were investigated. Steel 316 was chosen as the process material. A finite element model using the Abaqus commercial software was developed based on physical assumptions which divided the problem in two sequentially coupled cases of thermal and mechanical analyses. The predicted temperature profiles were verified through an experiment, which included SLM of thin walls that were instrumented by K-type thermocouples. The model assumptions (such as the constitutive material model, element type and size, etc.) were developed through various sensitivity investigations. Finally, a process parameter study was conducted through simulations and the results were compared with previous works. In the following the main aspects and conclusions are revisited.

5.1.1 Experiment—Thermocouples on Blades

A two phase SLM print was conducted for measuring in-situ temperatures. K-type thermocouples were attached to half-built thin structures through spot welding. The Measurements were done at 12 different spots with a maximum DAQ frequency of 4800Hz. The base plate was misaligned, but magnitudes up to 700°C were recorded. The temperature history was used to verify the thermal model.

5.1.2 Sensitivity Analysis—Model Assumptions

Various mesh sizes were used and optimal choice was made based on result accuracy and calculation time. A fully coupled thermo-mechanical analysis was conducted and shown not to differ from its sequential counterpart. Effect of a large substrate as for the first few layer in a real-world print was considered and stress concentration up to 700 MPa was observed. Fully integrated and reduced elements were both used for simulation and the model was found the be insensitive in this regard, but with lower calculation time with reduced integration elements. The perfectly plastic material definition was compared with isotropic hardening and the direct influence of hardening on residual stresses was observed. Anneal temperature was excluded from one simulation which led to very high stresses, thus showing the necessity of this consideration even though it does not directly represent physical concepts.

5.1.3 Simplified Model—Fast and Effective

The reference simulation was repeated without surrounding powder and with a simplified thermal solution. Instead of moving laser definition a liquid metal layer was deposited and held at melting point for the same duration of laser passage. Relatively similar stress distribution and values were seen, but with 80% reduction in calculation time.

5.1.4 Parametric Study—A Comparison with Literature

A new geometry with 3 layers and 3 tracks of 1 mm length in each layer was designed for parametric study. With constant laser energy density the scan speed and laser power were changed. No sensitivity was seen in average residual stresses similar to a previous work. By increasing the hatch space, the porosity of the printed area became larger and residual stresses dropped as expected. Preheating the substrate decreased the final residual stresses in the part, as it was confirmed by prior work.

5.2 Future Work

Finite element simulation in the field of selective laser melting still faces major limitations for application to process parameter optimization, or reliable residual stress and distortion prediction of real world parts. Some of these limitations are inherent to the complexity of the problem, but there are ways that can help improve these solutions. In this section, some suggestions for this purpose are made.

5.2.1 Further Model Verification

Employment of reliable material properties

In the model definition, material properties directly influence the output results. However, they were taken from external sources thus they do not apply for the stainless steel produced through SLM, and the process history and grain structure of the metal is different. Therefore, it is recommended to produce test pieces through the same methods of additive manufacturing, and conduct tensile, relaxation and other thermal or mechanical tests to extract the needed properties for finite element simulations. This way, the uncertainty due to material properties would be greatly reduced.

Residual stress measurement and mechanical model verification

Reliable measurement of residual stresses is more complex than temperature measurement which was done in this work. However, it is needed for confirming the assumptions made regarding the constitutive model and the mechanical analysis.

5.2.2 Further Sensitivity and Parametric Analysis

Creep consideration

At high temperatures, creep and relaxation become an important factor in the mechanical model. For the current work, there was no reliable source for creep data (most existing creep investigations are not valid for the short time frame of milliseconds). Thus one way to improve the model would be to measure the relaxation at different temperature levels for SLM samples and use them in a creep definition in the simulations.

Kinematic hardening consideration

The hardening model used here was isotropic while other works have used kinematic hardening or a combination of both types to predict material response beyond yield strength [57]. Once hardening data is available through tests, they can be used in different scenarios and the best model can be chosen based on comparison with residual stress measurements.

Effect of scanning strategy

A hot topic in current research is finding the ideal scanning strategy that minimizes the negative effects of localized heating due to laser beam exposure. Different scan strategies can be tested both in simulations and experiments, and their effects can be compared through residual stress measurements.

5.2.3 Further Development of Simplified Model

Simplifications of laser definition is inevitable for reducing calculation time and increasing model size. Following the successful residual stress predictions of the simplified model compared to the reference model, larger geometries with courses mesh size can be developed and used in stress prediction alongside experiments.

5.2.4 Evaluation of alternative FE packages

The latest version of Abaqus includes new features to facilitate additive manufacturing simulations. Additionally, other packages such as COMSOL have proven powerful in terms of modeling multiphysics phenomenon. Ansys is another commercial option which can be compared with available finite element simulation software packages in order to find the most efficient one in solving additive manufacturing simulation problems.

Appendix A

Subroutines

A.1 DFLUX

The DFLUX subroutine which was used for the reference model described in section 4.1 is presented below.

```
SUBROUTINE DFLUX(FLUX,SOL,KSTEP,KINC,TIME,NOEL,NPT,COORDS,
1 JLTYP,TEMP,PRESS,SNAME)
INCLUDE 'ABA_PARAM.INC'
DIMENSION FLUX(2), TIME(2), COORDS(3)
CHARACTER*80 SNAME

REAL*8 x_cur,y_cur,z_cur,stepno
x_cur=(INT(COORDS(1) * 1.D8 + 0.5)) / 1.D8
y_cur=(INT(COORDS(2) * 1.D8 + 0.5)) / 1.D8
z_cur=(INT(COORDS(3) * 1.D8 + 0.5)) / 1.D8
stepno=KSTEP

CALL LASER(x_cur,y_cur,z_cur,TIME(1),stepno,FLUX(1))

RETURN
END

SUBROUTINE LASER(x,y,z,time_input,stepno,HEAT)
INCLUDE 'ABA_PARAM.INC'
REAL*8,INTENT(IN)::
+        x,y,z,time_input,stepno
REAL*8,INTENT(OUT)::
+        HEAT
REAL*8 Radius,Absorb,Power,Velocity,Delta,Thickness,Length,
```

```
+        Q,Q0,Time_Trail,X0,Y0,Z0,layer_no
INTEGER          :: KSTEP = 0
PARAMETER (ZERO=0.D0,ONE=1.D0,TWO=2.D0,THREE=3.D0)

! Laser properties
Radius    = 5.D-5        ! laser radius
Absorb    = 3.D-1        ! laser absorption ratio
Power     = 100.D0       ! laser power
Velocity  = 2.D-1        ! scan speed
Delta     = 60.D-6       ! optical penetration depth
Thickness = 30.D-6       ! layer thickness
Length    = 1.D-3        ! Print length
Epsilon   = 1.D-9        ! 1 nanometer
Q0        = TWO*Absorb*Power/(3.1415926535D0*Radius**TWO*Delta)

Time_Trail= Length/Velocity      ! 1 mm print time
steptype  = Mod(KSTEP,2)         ! 1:heat 0:cool
layer_no  = KSTEP/2+1            ! number of current layer
KSTEP     = stepno

HEAT=ZERO

! Heating interval
IF (steptype.EQ.1) THEN
Z0=Thickness*layer_no   ! height of the current layer
ELSE ! Cooling interval
RETURN
END IF

! Laser location
X0=Velocity*time_input
Y0=ZERO

! Assigning heat flux inside the powder
IF (z.LE.Z0+Epsilon .AND. z.GT.Z0-Thickness-Epsilon) THEN
Q=Q0*exp(-TWO*((x-X0)**TWO+(y-Y0)**TWO)/Radius**TWO)*
+         exp((z-Z0)/Delta)
IF (Q/Q0 .GT. 1.D-1) THEN
HEAT=Q
END IF
END IF

RETURN
END
```

A.2 USDFLD

For switching the field variables the USDFLD subroutine was employed. The code which was used for the reference model is as follow.

```
SUBROUTINE USDFLD(FIELD,STATEV,PNEWDT,DIRECT,T,CELENT,
1 TIME,DTIME,CMNAME,ORNAME,NFIELD,NSTATV,NOEL,NPT,LAYER,
2 KSPT,KSTEP,KINC,NDI,NSHR,COORD,JMAC,JMATYP,MATLAYO,LACCFLA)
INCLUDE 'ABA_PARAM.INC'
CHARACTER*80 CMNAME,ORNAME
CHARACTER*3  FLGRAY(15)
DIMENSION FIELD(NFIELD),STATEV(NSTATV),DIRECT(3,3),
1 T(3,3),TIME(2)
DIMENSION ARRAY(15),JARRAY(15),JMAC(*),JMATYP(*),COORD(*)

REAL*8 temp_cur,Thickness,x_cur,y_cur,z_cur,
1       X1,Y1,X2,Y2,layer_no
PARAMETER (ZERO=0.D0,ONE=1.D0,TWO=2.D0,THREE=3.D0,
1 Temp_melt = 1.427D+3)
! Determination/reading of temperature
CALL GETVRM('TEMP',ARRAY,JARRAY,FLGRAY,JRCD,JMAC,JMATYP,
1 MATLAYO,LACCFLA)
temp_cur = ARRAY(1)

! Parameters
Thickness=30.D-6
X1=0.D0
Y1=-0.06D-3
X2=1.D-3
Y2=0.06D-3
x_cur=COORD(1)
y_cur=COORD(2)
z_cur=COORD(3)
steptype=Mod(KSTEP,2) ! 1:heat 0:cool
layer_no=KSTEP/2+1

! Step 1 initialization
IF (KINC.EQ.ONE .AND. KSTEP.EQ.ONE) THEN
IF (z_cur .LT. ZERO) THEN
IF (x_cur.GT.X1 .AND. x_cur.LT.X2
1      .AND. y_cur.GT.Y1 .AND. y_cur.LT.Y2) THEN
STATEV(1) = TWO ! Substrate Solid
ELSE
```

```
STATEV(1) = ONE ! Surrounding Powder
END IF
ELSE IF (z_cur .LT. Thickness) THEN
STATEV(1) = ONE ! Layer 1 Powder
END IF
! Step ODD initialization
ELSE IF (KINC.EQ.ONE .AND. steptype.EQ.1) THEN
IF (z_cur.GT.Thickness*(layer_no-ONE) .AND.
+       z_cur.LT.Thickness*layer_no) THEN
STATEV(1) = ONE ! Layer 2 Powder
END IF
END IF

IF (temp_cur.GT.Temp_melt .AND. STATEV(1).NE.ZERO) THEN
STATEV(1) = THREE       ! Liquid
ELSE IF (STATEV(1) .EQ. THREE) THEN
STATEV(1) = TWO ! Solid
END IF
FIELD(1) = STATEV(1)

RETURN
END
```

Bibliography

[1] Kaufui V. Wong and Aldo Hernandez. A Review of Additive Manufacturing. *ISRN Mechanical Engineering*, 2012:1–10, 2012.

[2] ASTM. STM F2792–10 Standard Terminology for Additive Manufacturing Technologies, 2009.

[3] Tuan D. Ngo, Alireza Kashani, Gabriele Imbalzano, Kate T. Q. Nguyen, and David Hui. Additive manufacturing (3d printing): A review of materials, methods, applications and challenges. *Composites Part B: Engineering*, 143:172–196, 2018.

[4] F Abe, E Costa Santos, Y Kitamura, K Osakada, and M Shiomi. Influence of forming conditions on the titanium model in rapid prototyping with the selective laser melting process. *Proceedings of the Institution of Mechanical Engineers, Part C: Journal of Mechanical Engineering Science*, 217(1):119–126, 2003.

[5] William E. Frazier. Metal Additive Manufacturing: A Review. *Journal of Materials Engineering and Performance*, 23(6):1917–1928, 2014.

[6] Steven Peters. A readiness level model for new manufacturing technologies. *Production Engineering*, 9(5-6):647–654, 2015.

[7] Andrew J. Pinkerton and Lin Li. Modelling the geometry of a moving laser melt pool and deposition track via energy and mass balances. *Journal of Physics D: Applied Physics*, 37(14):1885, 2004.

[8] Christoph Kenel, G Dasargyri, Thomas Bauer, A Colella, Adriaan Spierings, Christian Leinenbach, and Konrad Wegener. Selective laser melting of an oxide dispersion strengthened (ODS) gamma-TiAl alloy towards production of complex structures. *Materials & Design*, 134, 2017.

[9] Peter Mercelis and Jean-Pierre Kruth. Residual stresses in selective laser sintering and selective laser melting. *Rapid prototyping journal*, 12:254–265, 2006.

[10] Itziar Tolosa, Fermín Garciandía, Fidel Zubiri, Fidel Zapirain, and Aritz Esnaola. Study of mechanical properties of AISI 316 stainless steel processed by "selective laser melting", following different manufacturing strategies. *The International Journal of Advanced Manufacturing Technology*, 51(5):639–647, 2010.

[11] S. Leuders, M. Thöne, A. Riemer, T. Niendorf, T. Tröster, H. A. Richard, and H. J. Maier. On the mechanical behaviour of titanium alloy TiAl6v4 manufactured by selective laser melting: Fatigue resistance and crack growth performance. *International Journal of Fatigue*, 48:300–307, 2013.

[12] Christopher B. Williams, Farrokh Mistree, and David W. Rosen. A Functional Classification Framework for the Conceptual Design of Additive Manufacturing Technologies. *Journal of Mechanical Design*, 133(12):121002, 2011.

[13] C. Y. Yap, C. K. Chua, Z. L. Dong, Z. H. Liu, D. Q. Zhang, L. E. Loh, and S. L. Sing. Review of selective laser melting: Materials and applications. *Applied Physics Reviews*, 2(4):041101, 2015.

[14] Terry Wohlers and Tim Gornet. History of additive manufacturing. page 38, 2016.

[15] W Meiners, K Wissenbach, and A Gasser. Shaped body especially prototype or replacement part production. *DE Patent*, 19, 1998.

[16] Ranadip Acharya, Rohan Bansal, Justin J. Gambone, and Suman Das. A Coupled Thermal, Fluid Flow, and Solidification Model for the Processing of Single-Crystal Alloy CMSX-4 Through Scanning Laser Epitaxy for Turbine Engine Hot-Section Component Repair (Part I). *Metallurgical and Materials Transactions B*, 45(6):2247–2261, 2014.

[17] Ranadip Acharya, Rohan Bansal, Justin J. Gambone, and Suman Das. A Microstructure Evolution Model for the Processing of Single-Crystal Alloy CMSX-4 Through Scanning Laser Epitaxy for Turbine Engine Hot-Section Component Repair (Part II). *Metallurgical and Materials Transactions B*, 45(6):2279–2290, 2014.

[18] Ranadip Acharya, Rohan Bansal, Justin J. Gambone, Max A. Kaplan, Gerhard E. Fuchs, N. G. Rudawski, and Suman Das. Additive Manufacturing and Characterization of René 80 Superalloy Processed Through

Scanning Laser Epitaxy for Turbine Engine Hot-Section Component Repair. *Advanced Engineering Materials*, 17(7):942–950, 2015.

[19] Ranadip Acharya and Suman Das. Additive Manufacturing of IN100 Superalloy Through Scanning Laser Epitaxy for Turbine Engine Hot-Section Component Repair: Process Development, Modeling, Microstructural Characterization, and Process Control. *Metallurgical and Materials Transactions A*, 46(9):3864–3875, 2015.

[20] C. C. Ng, M. M. Savalani, H. C. Man, and I. Gibson. Layer manufacturing of magnesium and its alloy structures for future applications. *Virtual and Physical Prototyping*, 5(1):13–19, 2010.

[21] B. Ferrar, L. Mullen, E. Jones, R. Stamp, and C. J. Sutcliffe. Gas flow effects on selective laser melting (SLM) manufacturing performance. *Journal of Materials Processing Technology*, 212(2):355–364, 2012.

[22] I. Yadroitsev, A. Gusarov, I. Yadroitsava, and I. Smurov. Single track formation in selective laser melting of metal powders. *Journal of Materials Processing Technology*, 210(12):1624–1631, 2010.

[23] J. P. Kruth, L. Froyen, J. Van Vaerenbergh, P. Mercelis, M. Rombouts, and B. Lauwers. Selective laser melting of iron-based powder. *Journal of Materials Processing Technology*, 149(1):616–622, 2004.

[24] Ruidi Li, Jinhui Liu, Yusheng Shi, Li Wang, and Wei Jiang. Balling behavior of stainless steel and nickel powder during selective laser melting process. *The International Journal of Advanced Manufacturing Technology*, 59(9):1025–1035, 2012.

[25] Wayne E. King, Holly D. Barth, Victor M. Castillo, Gilbert F. Gallegos, John W. Gibbs, Douglas E. Hahn, Chandrika Kamath, and Alexander M. Rubenchik. Observation of keyhole-mode laser melting in laser powder-bed fusion additive manufacturing. *Journal of materials processing technology*, 214:2915–2925, 2014.

[26] Nikolay K. Tolochko, Yurii V. Khlopkov, Sergei E. Mozzharov, Michail B. Ignatiev, Tahar Laoui, and Victor I. Titov. Absorptance of powder materials suitable for laser sintering. *Rapid Prototyping Journal*, 6(3):155–161, 2000.

[27] P. Fischer, V. Romano, H. P. Weber, N. P. Karapatis, E. Boillat, and R. Glardon. Sintering of commercially pure titanium powder with a Nd:YAG laser source. *Acta Materialia*, 51(6):1651–1662, 2003.

[28] Choong S Kim. *Thermophysical properties of stainless steels*. Argonne National Laboratory Argonne, IL, USA, 1975.

[29] Maria Andreyevna Doubenskaia, Ivan Vladimirovich Zhirnov, Vladimir Ilyich Teleshevskiy, Philippe Bertrand, and Igor Yurievich Smurov. Determination of True Temperature in Selective Laser Melting of Metal Powder Using Infrared Camera, 2015.

[30] C. Li, J. F. Liu, and Y. B. Guo. Prediction of Residual Stress and Part Distortion in Selective Laser Melting. *Procedia CIRP*, 45:171–174, 2016.

[31] Wei Xing, Di Ouyang, Ning Li, Lin Liu, Wei Xing, Di Ouyang, Ning Li, and Lin Liu. Estimation of Residual Stress in Selective Laser Melting of a Zr-Based Amorphous Alloy. *Materials*, 11(8):1480, 2018.

[32] Jean-Pierre Kruth, Jan Deckers, Evren Yasa, and Ruben Wauthlé. Assessing and comparing influencing factors of residual stresses in selective laser melting using a novel analysis method. *Proceedings of the Institution of Mechanical Engineers, Part B: Journal of Engineering Manufacture*, 226(6):980–991, 2012.

[33] Yanjin Lu, Songquan Wu, Yiliang Gan, Tingting Huang, Chuanguang Yang, Lin Junjie, and Jinxin Lin. Study on the microstructure, mechanical property and residual stress of SLM Inconel-718 alloy manufactured by differing island scanning strategy. *Optics & Laser Technology*, 75:197–206, 2015.

[34] Luke N. Carter, Christopher Martin, Philip J. Withers, and Moataz M. Attallah. The influence of the laser scan strategy on grain structure and cracking behaviour in SLM powder-bed fabricated nickel superalloy. *Journal of Alloys and Compounds*, 615:338–347, 2014.

[35] M. Shiomi, K. Osakada, K. Nakamura, T. Yamashita, and F. Abe. Residual stress within metallic model made by selective laser melting process. *CIRP Annals*, 53(1):195–198, 2004.

[36] Jianfeng Sun, Yongqiang Yang, and Di Wang. Parametric optimization of selective laser melting for forming Ti6al4v samples by Taguchi method. *Optics & Laser Technology*, 49:118–124, 2013.

[37] Noriko Read, Wei Wang, Khamis Essa, and Moataz M. Attallah. Selective laser melting of AlSi10mg alloy: Process optimisation and mechanical properties development. *Materials & Design (1980-2015)*, 65:417–424, 2015.

[38] G. Casalino, S. L. Campanelli, N. Contuzzi, and A. D. Ludovico. Experimental investigation and statistical optimisation of the selective laser melting process of a maraging steel. *Optics & Laser Technology*, 65:151–158, 2015.

[39] Saad A. Khairallah and Andy Anderson. Mesoscopic simulation model of selective laser melting of stainless steel powder. *Journal of Materials Processing Technology*, 214(11):2627–2636, 2014.

[40] I. Yadroitsev, P. Krakhmalev, and I. Yadroitsava. Hierarchical design principles of selective laser melting for high quality metallic objects. *Additive Manufacturing*, 7:45–56, 2015.

[41] K. Dai and L. Shaw. Thermal and mechanical finite element modeling of laser forming from metal and ceramic powders. *Acta Materialia*, 52:69–80, 2004.

[42] Michael F. Zaeh and Gregor Branner. Investigations on residual stresses and deformations in selective laser melting. *Production Engineering*, 4:35–45, 2010.

[43] Bo Song, Shujuan Dong, Hanlin Liao, and Christian Coddet. Process parameter selection for selective laser melting of Ti6al4v based on temperature distribution simulation and experimental sintering. *The International Journal of Advanced Manufacturing Technology*, 61(9):967–974, 2012.

[44] Ahmed Hussein, Liang Hao, Chunze Yan, and Richard Everson. Finite element simulation of the temperature and stress fields in single layers built without-support in selective laser melting. *Materials & Design (1980-2015)*, 52:638–647, 2013.

[45] Donghua Dai and Dongdong Gu. Thermal behavior and densification mechanism during selective laser melting of copper matrix composites: Simulation and experiments. *Materials & Design*, 55:482–491, 2014.

[46] Tien T. Roehling, Sheldon S. Q. Wu, Saad A. Khairallah, John D. Roehling, S. Stefan Soezeri, Michael F. Crumb, and Manyalibo J. Matthews. Modulating laser intensity profile ellipticity for microstructural control during metal additive manufacturing. *Acta Materialia*, 128:197–206, 2017.

[47] Yu-Che Wu, Cheng-Hung San, Chih-Hsiang Chang, Huey-Jiuan Lin, Raed Marwan, Shuhei Baba, and Weng-Sing Hwang. Numerical modeling of melt-pool behavior in selective laser melting with random powder distribution and experimental validation. *Journal of Materials Processing Technology*, 254:72–78, 2018.

[48] A. J. Dunbar, E. R. Denlinger, J. Heigel, P. Michaleris, P. Guerrier, R. Martukanitz, and T. W. Simpson. Development of experimental method for in situ distortion and temperature measurements during the laser powder bed fusion additive manufacturing process. *Additive Manufacturing*, 12:25–30, 2016.

[49] Michele Chiumenti, Eric Neiva, Emilio Salsi, Miguel Cervera, Santiago Badia, Joan Moya, Zhuoer Chen, Caroline Lee, and Christopher Davies. Numerical modelling and experimental validation in Selective Laser Melting. *Additive Manufacturing*, 18:171–185, 2017.

[50] Ver Abaqus. 6.14 documentation. *Dassault Systemes Simulia Corporation*, 651, 2014.

[51] Karl-Heinz Leitz, Peter Singer, Arno Plankensteiner, Bernhard Tabernig, Heinrich Kestler, and Lorenz S. Sigl. Thermo-fluid dynamical simulation of layer build-up by selective laser melting of molybdenum and steel. *BHM Berg-und Hüttenmännische Monatshefte*, 162:172–178, 2017.

[52] John Goldak, Aditya Chakravarti, and Malcolm Bibby. A new finite element model for welding heat sources. *Metallurgical transactions B*, 15:299–305, 1984.

[53] Lien Chin Wei, Lili E. Ehrlich, Matthew J. Powell-Palm, Colt Montgomery, Jack Beuth, and Jonathan A. Malen. Thermal conductivity of metal powders for powder bed additive manufacturing. *Additive Manufacturing*, 21:201–208, 2018.

[54] Jie Yin, Haihong Zhu, Linda Ke, Panpan Hu, Chongwen He, Hu Zhang, and Xiaoyan Zeng. A finite element model of thermal evolution in laser micro sintering. *The International Journal of Advanced Manufacturing Technology*, 83(9-12):1847–1859, 2016.

[55] Djarot B. Darmadi, Anh Kiet-Tieu, and John Norrish. A validated thermo mechanical FEM model of bead-on-plate welding. *International Journal of Materials and Product Technology 15*, 48:146–166, 2014.

[56] P.C. Carnavas and N.W. Page. Elastic properties of compacted metal powders. *Journal of Materials Science*, 33(18):4647–4655, 1998.

[57] J. Mullins and J. Gunnars. Effect of hardening model on the weld residual stress field in pipe girth welds. 2009.

[58] Meysam Naghizadeh and Hamed Mirzadeh. Microstructural Evolutions During Reversion Annealing of Cold-Rolled AISI 316 Austenitic Stainless Steel. *Metallurgical and Materials Transactions A*, 49(6):2248–2256, 2018.

[59] Guido Dhondt. Calculix crunchix user's manual version 2.7. `http://web.mit.edu/calculix_v2.7/CalculiX/ccx_2.7/doc/ccx/node25.html`. Accessed: 2018-09-21.

[60] Jun Cao, Fencheng Liu, Xin Lin, Chunping Huang, Jing Chen, and Weidong Huang. Effect of overlap rate on recrystallization behaviors of Laser Solid Formed Inconel 718 superalloy. *Optics & Laser Technology*, 45:228–235, 2013.

[61] Johannes Trapp, Alexander M. Rubenchik, Gabe Guss, and Manyalibo J. Matthews. In situ absorptivity measurements of metallic powders during laser powder-bed fusion additive manufacturing. *Applied Materials Today*, 9:341–349, 2017.

ETH
Eidgenössische Technische Hochschule Zürich
Swiss Federal Institute of Technology Zurich

Declaration of originality

The signed declaration of originality is a component of every semester paper, Bachelor's thesis, Master's thesis and any other degree paper undertaken during the course of studies, including the respective electronic versions.

Lecturers may also require a declaration of originality for other written papers compiled for their courses.

I hereby confirm that I am the sole author of the written work here enclosed and that I have compiled it in my own words. Parts excepted are corrections of form and content by the supervisor.

Title of work (in block letters):

Authored by (in block letters):
For papers written by groups the names of all authors are required.

Name(s):	**First name(s):**

With my signature I confirm that
- I have committed none of the forms of plagiarism described in the 'Citation etiquette' information sheet.
- I have documented all methods, data and processes truthfully.
- I have not manipulated any data.
- I have mentioned all persons who were significant facilitators of the work.

I am aware that the work may be screened electronically for plagiarism.

Place, date	**Signature(s)**

For papers written by groups the names of all authors are required. Their signatures collectively guarantee the entire content of the written paper.